# Quantitative Evaluation of Ocean Surface Spectral Model Influence on Sea Surface Backscattering

J.T. Johnson and C.W. Chuang

# REPORT DOCUMENTATION PAGE

| 1. AGENCY USE ONLY (Leave blank) | 2. REPORT DATE September 2000 | 3. REPORT TYPE AND DATES COVERED Technical Report |
|---|---|---|

**4. TITLE AND SUBTITLE**
Quantitative Evaluation of Ocean Surface Spectral Model Influence on Sea Surface Backscattering

**5. FUNDING NUMBERS**
Grant N00014-00-1-0349

**6. AUTHOR(S)**
J.T. Johnson and C.W. Chuang

**7. PERFORMING ORGANIZATION NAME(S) AND ADDRESS(ES)**
The Ohio State University
ElectroScience Laboratory
1320 Kinnear Road
Columbus, OH 43212

**8. PERFORMING ORGANIZATION REPORT NUMBER**
738927-1

**9. SPONSORING/MONITORING AGENCY NAME(S) AND ADDRESS(ES)**
Office of Naval Research
Ballston Centre Tower One
800 North Quincy Street
Arlington, VA 22217-5660

**10. SPONSORING/MONITORING AGENCY REPORT NUMBER**

**11. SUPPLEMENTARY NOTES**

**12a. DISTRIBUTION/AVAILABILITY STATEMENT**
A. Approved for public release;
Distribution is unlimited

**12b. DISTRIBUTION CODE**

**13. ABSTRACT** (Maximum 200 words)

Sea surface backscattering in the microwave region is evaluated for three ocean surface wavenumber spectral models using the composite surface method. The three ocean surface spectral models considered are a power law spectrum, the Durden-Vesecky spectrum and the Apel spectrum. Backscattering results obtained for the power law spectrum are found to be in good agreement with those calculated using a small slope approximation method. Backscattering results obtained for the Durden-Vesecky and Apel spectral models are also compared with three empirical scattering models (CMOD2-I3, SASS-II and NSCAT-I). In general, the empirical scattering models fall between the predictions of the Durden-Vesecky and Apel spectra.

**14. SUBJECT TERMS**

**15. NUMBER OF PAGES**
46

**16. PRICE CODE**

| 17. SECURITY CLASSIFICATION OF REPORT | 18. SECURITY CLASSIFICATION OF THIS PAGE | 19. SECURITY CLASSIFICATION OF ABSTRACT | 20. LIMITATION OF ABSTRACT |
|---|---|---|---|
| Unclassified | Unclassified | Unclassified | UL |

# Acknowledgment

# Contents

# List of Figures

# Chapter 1

# Introduction

Accurate knowledge of the sea surface directional spectrum is important for oceano-graphic and remote sensing applications. For example, the sea surface directional spectrum is used in the composite surface model to predict sea surface backscattering, and various sea surface directional spectral models may yield very different backscattering results. It is the purpose of this report to evaluate sea surface backscattering in the microwave region for three surface directional spectra using the composite surface method.

The composite surface model has been proven to be a powerful and efficient tool for obtaining useful quantitative sea surface backscattering results [1]-[5]. Under the composite surface (or two-scale) model, the ocean surface spectrum is separated into long and short wave regions (relative to the electromagnetic wavelength) through choice of a separation wavenumber, typically chosen as 2 to 3 electromagnetic wavelengths. Near normal incidence radar returns are described in this method according to geometrical optics, while oblique incidence radar cross sections are obtained by averaging small perturbation method predictions over the slope distribution of the long wave spectral region. The method has limitations as near grazing incidence geometries are approached, but should provide accurate predictions for grazing angles approximately ten degrees or larger [6].

The three sea surface wavenumber spectral models investigated in this report are a power law spectrum, the Durden-Vesecky spectrum [7] and the Apel spectrum [8]. The power law spectrum describes a sea surface which does not vary with the wind velocity over the sea surface. Although it is not a realistic description of the sea surface, its simplicity is utilized to demonstrate the viability of the composite surface

method to predict the sea surface backscattering. This is done by comparing results obtained from the composite surface method with those obtained from the small slope approximation for rough surface scattering [9]. The small slope approximation is a completely different method from the composite surface method for calculating sea surface scattering. The former does not require a separation of the spectrum into long and short wave regions, but it is not as efficient as the latter in terms of the amount of computations required. Because they are two completely different methods, agreement between results obtained by them should indicate the applicabilities of both methods.

Unlike the power law spectrum, the Durden-Vesecky and Apel spectra do vary with the wind velocity over the sea surface. The differences between the latter two spectra lie primarily in the short wave portion of the spectrum and the azimuthal variations of the spectrum. One glaring difference between them is observed in the fact that the Durden-Vesecky model places all azimuthal variations in short gravity-capillary and capillary waves only, while the Apel model places azimuthal variations in both long and short waves. Thus the Durden-Vesecky and Apel spectra are good candidates for studying sea surface directional spectral model influence on sea surface backscattering. Because they describe more realistic sea surfaces, backscattering results obtained for these two spectra can be compared with empirical scattering models available in the literature. Expressions for an additional surface spectral model recently developed by the Naval Research Laboratory [10]-[11] are also included, but scattering calculations with this model have not yet been completed.

Chapter 2 of this report considers the expressions needed for application of the composite surface method and reviews the surface spectral models considered. Sea surface backscattering results obtained from the composite surface method with the power law spectrum are then compared with those obtained from the small slope approximation in Chapter 3. Comparisons of backscattering results at 1 GHz, 5 GHz, 10 GHz, 14 GHz and 35 GHz for the Durden-Vesecky and Apel spectra with wind speeds ranging from 4 m/sec to 20 m/sec at a height of 19.5 m above the sea surface are given in Chapter 4. Backscattering results at 5 GHz and 14 GHz are also compared with three empirical scattering models (CMOD2-I3, SASS-II, and NSCAT-I) in Chapter 4.

# Chapter 2

# The Composite Surface Method And Sea Surface Spectral Models

This chapter briefly reviews the formulation of the composite surface method for calculating the backscattered radar cross sections from a sea surface, and also provides expressions for the sea surface spectral models considered in the study.

## 2.1 Composite Surface Method

As mentioned in the previous chapter, the composite surface method separates the sea surface wavenumber spectrum into long and short wave regions (relative to the electromagnetic wavelength). In this report, the separation wavenumber is chosen to be one half of the incident electromagnetic wavenumber, which has been shown to yield favorable scattering results compared to those obtained by a rigorous numerical method [12]. Near normal incidence, the long wave spectral region yields specular returns according to geometrical optics, while oblique incidence radar returns are obtained by averaging small perturbation method predictions (Bragg scattering from the short wave spectral region) over the slope distribution of the long wave spectral region.

Let $W(k_x, k_y)$ denote the sea surface wavenumber spectrum. For simplicity, the $x$-axis and $y$-axis are in the up-wind and cross-wind directions, respectively, with the $z$-axis pointing upward from the sea surface. The slope variances of the sea surface in the up-wind and cross-wind directions due to its long wave spectral region are given,

respectively, by

$$s_x^2 = \int_0^{\frac{1}{2}k} dk_\rho \int_0^{2\pi} d\phi \; k_\rho^3 \cos^2 \phi \, W(k_\rho \cos \phi, k_\rho \sin \phi) \qquad (2.1)$$

$$s_y^2 = \int_0^{\frac{1}{2}k} dk_\rho \int_0^{2\pi} d\phi \; k_\rho^3 \sin^2 \phi \, W(k_\rho \cos \phi, k_\rho \sin \phi) \qquad (2.2)$$

where $k$ is the wavenumber of the incident electromagnetic wave, $k_\rho \cos \phi = k_x$ and $k_\rho \sin \phi = k_y$.

The specular radar return due to the long wave spectral region of the sea surface spectrum, assuming a Gaussian slope distribution, is given by

$$\sigma = \frac{|\Gamma|^2}{2 \cos^4 \theta_i \, s_x s_y} \, e^{-\frac{1}{2} \tan^2 \theta_i \left[ \frac{\cos^2 \phi_i}{s_x^2} + \frac{\sin^2 \phi_i}{s_y^2} \right]} \qquad (2.3)$$

where $\sigma$ is the normalized radar cross section, $(\theta_i, \phi_i)$ are the incident polar and azimuthal angles with $\theta_i$ measured from the $z$-axis, and $|\Gamma|^2$ is the power reflection coefficient from a calm sea surface at normal incidence,

$$|\Gamma|^2 = \left| \frac{1 - \sqrt{\epsilon}}{1 + \sqrt{\epsilon}} \right|^2 \qquad (2.4)$$

with $\epsilon$ being the relative dielectric constant of the sea. A higher order correction to $\Gamma$, which is small, has been omitted in (2.4). The expression in (2.3) is valid for both horizontal and vertical polarizations. It is seen from (2.3) that the specular radar return drops quickly as the incident angle $\theta_i$ increases. Thus (2.3) is significant only for near normal incidence.

The expressions for the Bragg scattering radar cross sections from a tilted sea surface are considered next. Define a primed coordinate system such that the $x'$- and $y'$-axes are in and perpendicular to the plane of incidence, respectively; i.e. the $x'y'$ coordinate system is obtained by rotating the $xy$ coordinate system by the angle $\phi_i$ about the $z$ axis. The tilted sea surface is defined by two angles, $\psi$ and $\delta$. The angle $\psi$ is obtained by rotating the untilted sea surface normal ($z$- or $z'$-axis) about the $y'$-axis resulting in a double primed ($x''y''z''$) coordinate system, and the angle $\delta$ is obtained by rotating the new surface normal ($z''$-axis) about the $x''$-axis. The incident angle with respect to the tilted surface becomes $\theta_i'$, which is related to $\theta_i$ by

$$\cos \theta_i' = \cos(\theta_i + \psi) \cos \delta. \qquad (2.5)$$

4

Now, according to the small perturbation method, the Bragg scattering radar cross sections are given by [13]

$$\sigma^0_{HH}(\theta'_i) = 16\pi k^4 \cos^4 \theta'_i \left| \left( \frac{\alpha \cos \delta}{\sin \theta'_i} \right)^2 g^{(1)}_{\perp\perp}(\theta'_i) + \left( \frac{\sin \delta}{\sin \theta'_i} \right)^2 g^{(1)}_{\| \|}(\theta'_i) \right|^2 W(k'_x, k'_y) \quad (2.6)$$

$$\sigma^0_{VV}(\theta'_i) = 16\pi k^4 \cos^4 \theta'_i \left| \left( \frac{\alpha \cos \delta}{\sin \theta'_i} \right)^2 g^{(1)}_{\| \|}(\theta'_i) + \left( \frac{\sin \delta}{\sin \theta'_i} \right)^2 g^{(1)}_{\perp\perp}(\theta'_i) \right|^2 W(k'_x, k'_y) \quad (2.7)$$

$$g^{(1)}_{\perp\perp}(\theta'_i) = \frac{\epsilon - 1}{(\cos \theta'_i + \sqrt{\epsilon - \sin^2 \theta'_i})^2} \quad (2.8)$$

$$g^{(1)}_{\| \|}(\theta'_i) = \frac{\epsilon - 1}{(\epsilon \cos \theta'_i + \sqrt{\epsilon - \sin^2 \theta'_i})^2} \left[ \epsilon(1 + \sin^2 \theta'_i) - \sin^2 \theta'_i \right] \quad (2.9)$$

$$k'_x = 2k(\alpha \cos \phi_i - \gamma \sin \delta \sin \phi_i) \quad (2.10)$$

$$k'_y = 2k(\alpha \sin \phi_i + \gamma \sin \delta \cos \phi_i) \quad (2.11)$$

$$\alpha = \sin(\theta_i + \psi) \quad (2.12)$$

$$\gamma = \cos(\theta_i + \psi) \quad (2.13)$$

The expressions in (2.6) and (2.7) are, respectively, copol normalized radar cross sections for the horizontal and vertical polarizations. Note that $W(k'_x, k'_y)$ in (2.6) and (2.7) should be set to zero if $\left(k'^2_x + k'^2_y\right)^{1/2} < \frac{1}{2}k$ as in the cases of near normal incidence, which means that (2.6) and (2.7) are significant only for oblique incidence and are the contributions of the short wave spectral region of the sea surface spectrum. These radar returns, (2.6) and (2.7), should be averaged over the slope distribution of the long wave spectral region. Assuming a Gaussian slope distribution, the averaged radar cross sections for $\phi_i = 0$ or $\pi/2$ are

$$\left\{ \begin{array}{c} \sigma_{HH}(\theta_i) \\ \sigma_{VV}(\theta_i) \end{array} \right\} = \int_{-\infty}^{\infty} dz_x \int_{-\infty}^{\infty} dz_y \left\{ \begin{array}{c} \sigma^0_{HH}(\theta'_i) \\ \sigma^0_{VV}(\theta'_i) \end{array} \right\} \frac{1}{2\pi s_x s_y} e^{-\frac{1}{2}\left[ \left( \frac{z_x}{s_x} \right)^2 + \left( \frac{z_y}{s_y} \right)^2 \right]} \quad (2.14)$$

where $(z_x = \tan \psi, z_y = \tan \delta)$ for $\phi_i = 0$ and $(z_x = \tan \delta, z_y = \tan \psi)$ for $\phi_i = \pi/2$. The above integration is performed numerically using Gauss-Legendre quadrature. Because of the Gaussian distribution, the integration ranges in (2.14) can be truncated to $|z_x| < 4s_x$ and $|z_y| < 4s_y$.

For the cross polarized radar return calculation, a strict application of the composite surface method would require adding first and second order small perturbation results for a tilted sea surface averaged over the long wave slope distribution. These

5

calculations would require a prohibitive amount of computation. Instead, a simple second order small perturbation solution for an untilted sea surface as obtained by Valenzuela [14] will be used as follows:

$$
\sigma_{HV}(\theta_i) = 8\pi k^4 \cos^2 \theta_i \left| \frac{2(k_1^2 - k^2)^2 k_{1zi} k_{zi}}{(k_{1zi} + k_{zi})(k_1^2 k_{zi} + k^2 k_{1zi})} \right|^2
$$
$$
\int_{-\infty}^{\infty} dk_x \int_{-\infty}^{\infty} dk_y \left| \frac{(k_{xi} k_y - k_{yi} k_x)(k_{xi} k_x + k_{yi} k_y)}{(k_{xi}^2 + k_{yi}^2)(k_1^2 k_z + k^2 k_{1z})} \right|^2
$$
$$
W(k_x - k_{xi}, k_y - k_{yi}) W(k_x + k_{xi}, k_y + k_{yi}) \tag{2.15}
$$

where

$$
k_1^2 = \epsilon k^2 \tag{2.16}
$$
$$
k_{xi} = k \sin\theta_i \cos\phi_i, \quad k_{yi} = k \sin\theta_i \sin\phi_i, \quad k_{zi} = k \cos\theta_i \tag{2.17}
$$
$$
k_{1zi} = (k_1^2 - k_{xi}^2 - k_{yi}^2)^{1/2} \tag{2.18}
$$
$$
k_z = (k^2 - k_x^2 - k_y^2)^{1/2} \tag{2.19}
$$
$$
k_{1z} = (k_1^2 - k_x^2 - k_y^2)^{1/2} \tag{2.20}
$$

With the substitution of $k_x = k_\rho \cos\phi$ and $k_y = k_\rho \sin\phi$, (2.15) becomes

$$
\sigma_{HV}(\theta_i) = 8\pi k^4 \cos^4 \theta_i \left| \frac{(\epsilon - 1)^2 \sqrt{\epsilon - \sin^2 \theta_i}}{(\cos\theta_i + \sqrt{\epsilon - \sin^2 \theta_i})(\epsilon \cos\theta_i + \sqrt{\epsilon - \sin^2 \theta_i})} \right|^2
$$
$$
\cdot \int_0^\infty dk_\rho \int_0^{2\pi} d\phi \frac{k_\rho^5 \sin^2 2(\phi - \phi_i)}{|\epsilon k_z + k_{1z}|^2}
$$
$$
W(k_x - k_{xi}, k_y - k_{yi}) W(k_x + k_{xi}, k_y + k_{yi}) \tag{2.21}
$$

Note the integrals above are over the entire surface spectrum so that both long and short wave contributions are included; a validation of the above procedure will be provided in Chapter 3 through comparison with the small slope approximation. Again the required numerical integration is performed using Gauss-Legendre quadrature.

## 2.2 Sea Surface Spectral Models

The formulation of the composite surface method given above will be used to evaluate radar returns from a rough sea surface for three sea surface wavenumber spectral models: a power law model, the Durden-Vesecky model and the Apel model. The

6

power law spectral model is described by

$$W(k_\rho \cos\phi, k_\rho \sin\phi) = a_0/k_\rho^4 \qquad (2.22)$$

where $a_0 = \frac{0.004}{2\pi}$. This simple spectral model does not vary with the wind velocity or azimuthal angle and is primarily used to validate the composite surface method by comparing scattering results with those obtained from the small slope approximation.

The Durden-Vesecky spectrum was derived in [7] to match sea surface backscattered data under a composite surface model, and thus is not derived from direct hydrodynamic measurements. The spectrum is described by

$$W(k_\rho \cos\phi, k_\rho \sin\phi) = \frac{a_1}{2\pi k_\rho^4}[1 + C(1 - e^{-ss\cdot k_\rho^2})\cos 2\phi]$$

$$\cdot \begin{cases} e^{-0.74\left(\frac{9.81}{u_{19.5}^2 k_\rho}\right)^2} & , \text{ for } k_\rho < 2 \\ \left(\frac{bk_\rho u_*^2}{g}\right)^{a\log_{10}(k_\rho/2)} & , \text{ for } k_\rho > 2 \end{cases} \qquad (2.23)$$

The various parameters in (2.23) are defined as follows:

$$a_1 = 0.004,$$

$$ss = 1.5 \times 10^{-4},$$

$$b = 1.25,$$

$$a = 0.225,$$

$$g = 9.81 + 7.25 \times 10^{-5}k_\rho^2,$$

$$C = \frac{2(1-R)}{1+R}\frac{1}{1-d},$$

$$R = \frac{0.003 + 0.00192u_{12.5}}{0.00316u_{12.5}},$$

$$d = \frac{\int_0^\infty dk_\rho k_\rho^2 s(k_\rho)e^{-ss\cdot k_\rho^2}}{\int_0^\infty dk_\rho\, k_\rho^2 s(k_\rho)},$$

$$s(k_\rho) = \frac{k_\rho W(k_\rho\cos\phi, k_\rho\sin\phi)}{1 + C(1 - e^{-ss\cdot k_\rho^2})\cos 2\phi}.$$

Also note that $u_*$ is the surface friction velocity in $m/s$ and the wind velocity $u_h$ at a height $h$ (in meters) above the sea surface is related to $u_*$ by

$$u_h = \frac{u_*}{0.4}\left[\ln\frac{h}{6.84 \times 10^{-5}/u_* + 4.28 \times 10^{-3}u_*^2 - 4.43 \times 10^{-4}}\right]$$

The Apel spectrum was derived in [8] to match measured buoy long wave spectra and measured wave tank short wave spectra, and thus has a more direct connection

to hydrodynamic data. However, other researchers have criticized slope moments obtained from this spectrum, as well as the large amplitudes predicted near the gravity-capillary wave phase speed minimum [15]. The model is described by

$$
\begin{aligned}
W(k_\rho \cos\phi, k_\rho \sin\phi) = \; & A\frac{a_2}{k_\rho^4} e^{-[0.14+5(k_p/k_\rho)^{1.3}]\phi^2} e^{-(k_p/k_\rho)^2 - (k_\rho/6283)^2} \\
& 1.7^{[e^{-(\sqrt{k_\rho}-\sqrt{k_p})^2/0.32 k_p}]} \left\{ \frac{1}{1+(k_\rho/100)^2} + 10^{[-4.95+3.45(1-e^{-u_{10}/4.7})]} \right. \\
& \left. \left[ 0.8 k_\rho \; \mathrm{sech} \; \left( \frac{k_\rho - 400}{450} \right) \right] \right\}, \quad \text{for } 0 < \phi < \pi/2 \quad (2.24)
\end{aligned}
$$

where $a_2 = 0.00195$ and $k_p = \frac{9.81}{\sqrt{2} u_{10}^2}$ . Note that (2.24) is valid for $0 < \phi < \pi/2$. The spectrum in the other quadrants is generated by reflecting (2.24) about the x- and y-axes. The factor $A$ in (2.24) is introduced to keep the surface height variance constant. $A$ is given by

$$
A = \frac{1}{2} \; \mathrm{erf} \; \left[ \pi \sqrt{0.14 + 5(k_p/k_\rho)^{1.3}} \right] \Big/ \; \mathrm{erf} \; \left[ \frac{\pi}{2} \sqrt{0.14 + 5(k_p/k_\rho)^{1.3}} \right]
$$

where erf is the error function.

A final model developed from hydrodynamic measurements by the Naval Research Laboratory [10]-[11] is also considered and will be included in future comparisons of scattering measurements. The NRL model provides a one-dimensional surface spectrum which can be extended to two dimensions if a form for surface azimuthal variations is assumed. If a uniform $\cos^2\phi$ variation is assumed for simplicity, the resulting two dimensional spectrum is

$$
W(k_\rho \cos\phi, k_\rho \sin\phi) = u_* \cos^2\phi \begin{cases} \frac{5.02\times10^{-3}}{1.21} k_\rho^{-3.5} & \frac{g}{U_{10}^2} < k_\rho < 16 \\ \frac{2.01\times10^{-2}}{1.19} k_\rho^{-4} & 16 < k_\rho < 100 \\ \frac{1.97\times10^{-3}}{1.19} k_\rho^{-3} \frac{1}{g+\tau k^2} & 100 < k_\rho < 900 \\ \frac{2.57\times10^4}{1.1} k_\rho^{-6} & 900 < k_\rho < 1600 \end{cases} \quad (2.25)
$$

where $k$ is in $rads/m$, $g$ is the acceleration of gravity, and $\tau$ is the ratio of water surface tension to its density. The above form is based on tests which insure that an integration of the two dimensional spectrum over $k_y$ approximates the original one-dimensional NRL spectrum. Inclusion of recently proposed azimuthal distributions for this spectrum [16]-[17] are currently under consideration.

8

## 2.2.1 Comparison of Spectral Models

To compare spectra predicted by the Durden-Vesecky, Apel, and NRL models, approximate the directional spectrum by

$$W(k_\rho \cos\phi, k_\rho \sin\phi) \approx W_0(k_\rho) + W_2(k_\rho)\cos 2\phi. \qquad (2.26)$$

Figures 2.1-2.3 show the comparisons of the corresponding zeroth and second harmonic curvature spectra, i.e., $c_0(k_\rho) = k_\rho^4 W_0(k_\rho)$ and $c_2(\rho) = k_\rho^4 W_2(k_\rho)$, at three wind speeds. While the three models show agreement in the zeroth harmonic to within approximately an order of magnitude, there are significant differences. The NRL model is observed to predict the largest amplitudes in the $10 < k < 100$ range for the higher wind speeds, and to have a peak for $k > 100$ which is similar to that of the Apel spectrum. Both the NRL and Apel models typically predict larger spectral amplitudes than the Durden-Vesecky model, except for very small or very large wavenumbers. The second harmonic term is responsible for azimuthal variation in the spectrum. One can see that the Durden-Vesecky model places all azimuthal variations in the short wave region, while the Apel model has azimuthal variations in both long and short wave regions. Second harmonics for the NRL model are not plotted due to the simple $\cos^2\phi$ assumption used.

The directional spectrum at the Bragg scattering wavenumber is important as it influences oblique incidence radar cross sections. The Bragg scattering wavenumber is $2k\sin\theta_i$, which depends on the incident frequency and incident angle. Figure 2.4 shows the comparisons of $W(2k\sin\pi/4, 0)$ for the Durden-Vesecky, Apel, and NRL spectral models at five frequencies. These comparisons show the NRL model to predict significantly larger Bragg wavenumber amplitudes for the frequencies considered, except at the highest frequency where Apel spectrum results are similar. The Apel model amplitudes are larger than those of the Durden-Vesecky model, with the greatest degree of similarity of 5 GHz. These results suggest that copol radar returns at oblique incidence will be significantly larger with the NRL spectral model than with the Apel and Durden-Vesecky models, and somewhat larger for the Apel model than the Durden-Vesecky model. Detailed comparisons of scattering cross sections for the Apel and Durden-Vesecky spectra are presented in Chapter 4.
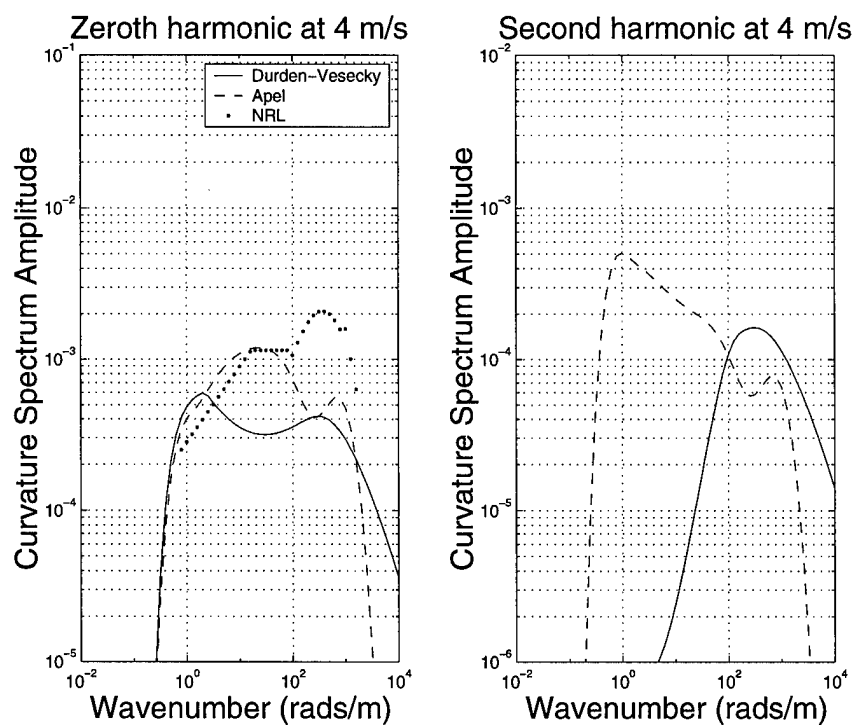
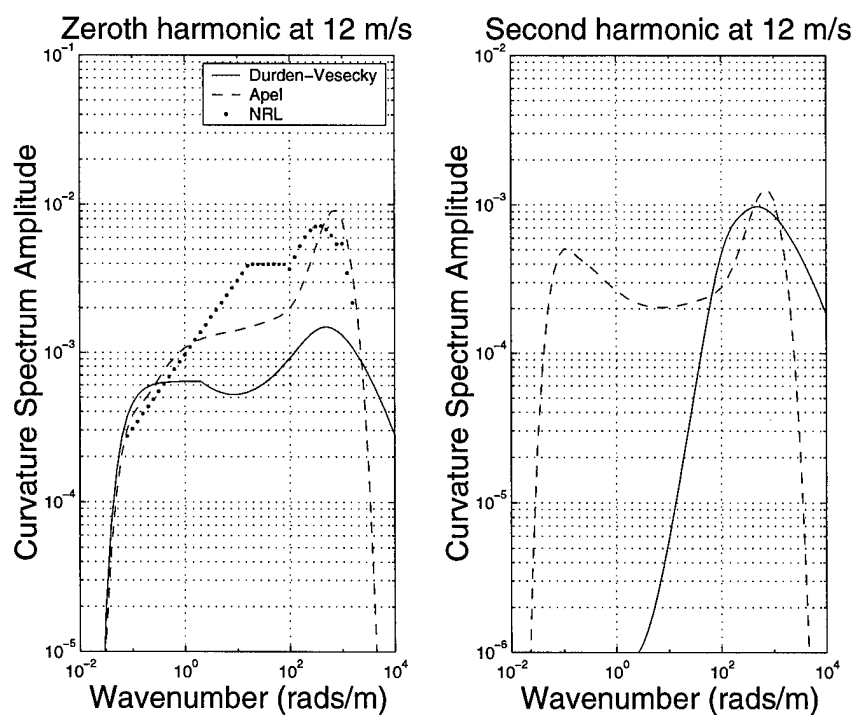Figure 2.1: Comparisons of curvature spectra at $u_{19.5} = 4$ m/sec.



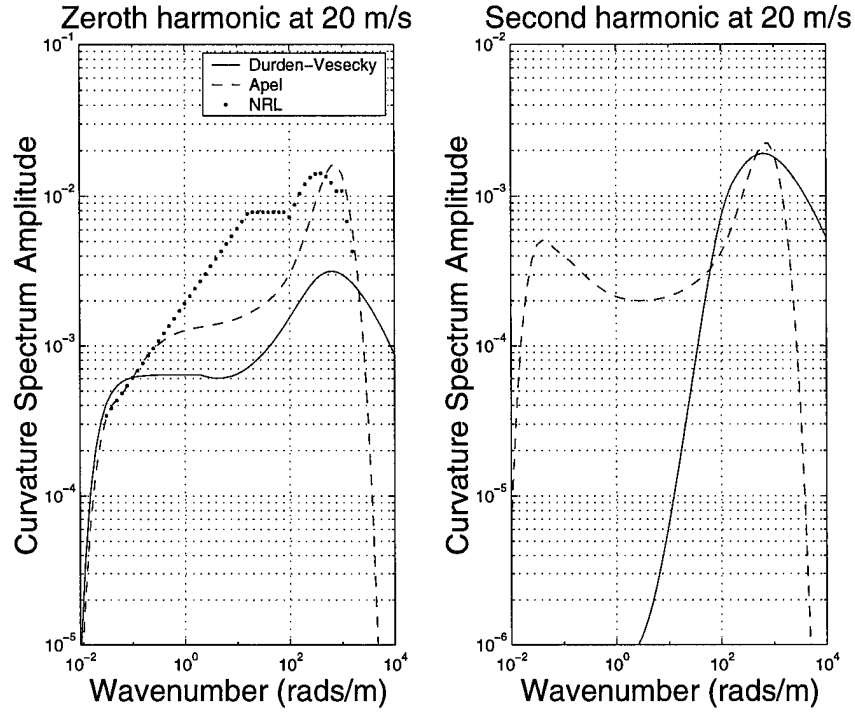Figure 2.2: Comparisons of curvature spectra at $u_{19.5} = 12$ m/sec.

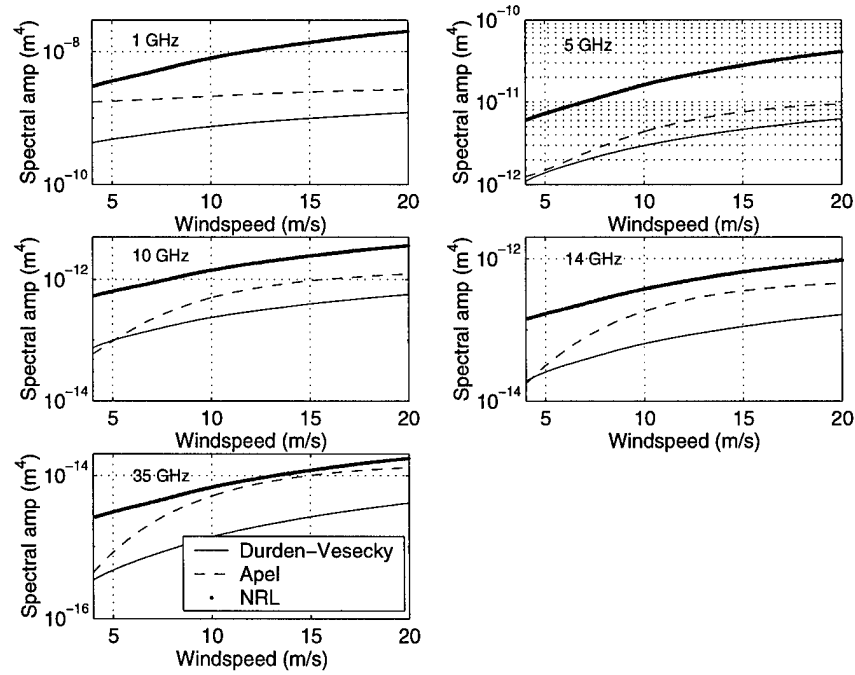Figure 2.3: Comparisons of curvature spectra at $u_{19.5} = 20$ m/sec.



Figure 2.4: Comparisons of $W(2k\sin\theta_i, 0)$ for $\theta_i = \pi/4$

11

# Chapter 3

# Radar Cross Sections for the Power Law Spectrum

As a test of the applicability of the composite surface model, backscattering results are compared in this chapter with those obtained from the small slope approximation [9]. The small slope approximation (SSA) is a more rigorous theory of rough surface scattering which can include both large and small scale roughness without choice of an arbitrary separation wavenumber in the spectrum. The SSA is based on a perturbation expansion in surface "quasi-slope", with the zeroth order term producing an expression for average cross sections similar to that obtained from the Kirchhoff approximation with a modified polarization dependence outside of the surface integration. Calculation of the first order correction to zeroth order results requires an additional integration over the surface Fourier transform, thus increasing computational requirements. Because SSA expressions are more difficult to evaluate than those of the composite model, use of the composite model is more efficient if it can be shown that the two models yield similar results. The relationship between the first order SSA and the composite model has been considered in [18], where it is shown that the two should yield similar predictions if the first order SSA correction is included.

To simplify SSA model calculations, a power law spectrum is used in the comparison. Since the power law spectrum does not vary with wind speed or azimuth angle, the number of parameters in the comparison is substantially reduced. Note that the simple power law wavenumber spectrum given in equation (2.22) grows without bound as $k_\rho$ approaches zero. Thus it is necessary to impose a low cutoff wavenumber such that the spectrum exists only for $k_\rho > k_{\text{cutoff}}$. Variations in backscattering

cross sections with frequency can also be neglected in this comparison if the cutoff wavenumbers chosen are described relative to the electromagnetic wavenumber $k$.

To avoid difficulties in first order SSA model calculations, a Monte Carlo evaluation of SSA cross sections with 100 realizations was performed following the deterministic surface method of [19]. Since the deterministic surfaces generated are of finite size, the maximum surface size and thus minimum low cutoff wavenumber are limited by computational capacity. The results shown used 512 by 512 point surfaces of size 128 by 128 electromagnetic wavelengths. Two comparisons using low cutoff wavenumbers $k/128$ and $k/64$ are performed to examine the effect of increasing surface low frequency content. For surface rms height $h$, the resulting $kh$ products are 5.7 and 2.9 respectively so that surfaces can be considered moderately rough on an electromagnetic scale. Surface permittivities are chosen to model sea water at 14 GHz.

Backscattered radar cross sections for low cutoff wavenumber $k/128$ (2.25 rad/m at 14 GHz) calculated using the composite surface method are compared with those obtained by the small slope approximation in Figure 3.1. The agreement between the two is very good for all observation angles in co-polarized results, indicating the applicability of the composite model. Predictions of cross polarized radar returns obtained using equation (2.21) also match SSA results well, except for $\theta_i < 10°$ where SSA results are over predicted. Similar conclusions are also observed when the low cutoff wavenumber is set at $k/64$ (4.5 rad/m at 14 GHz) as shown in Figure 3.2. Comparison of Figures 3.1 and 3.2 shows the expected effect of increasing surface low frequency content: cross sections decrease near normal incidence while increasing at larger observation angles. Overall, these results indicate the applicability of both the composite and SSA methods for calculating the radar cross sections from a rough sea surface, and motivate use of the composite model for larger scale studies of sea surface backscattering.
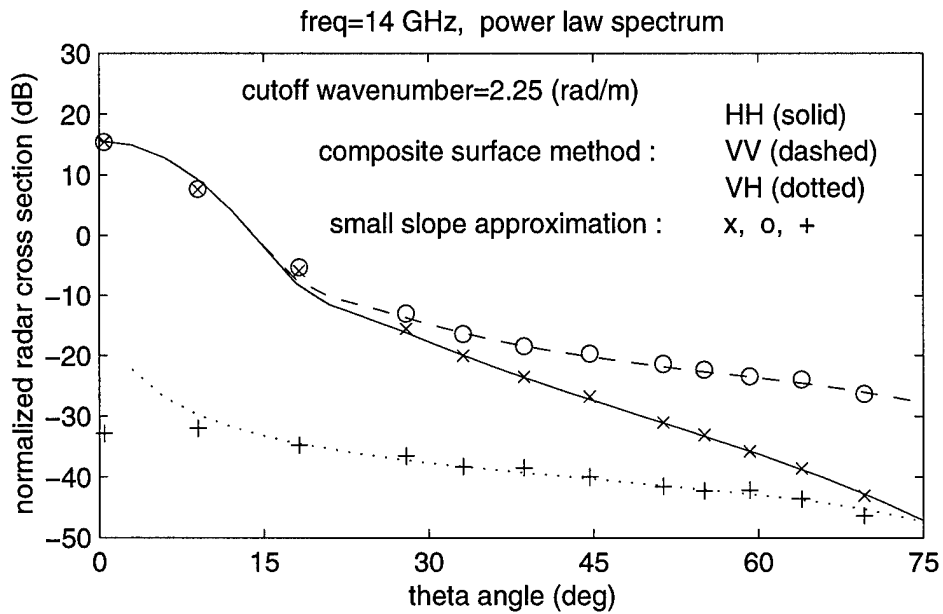
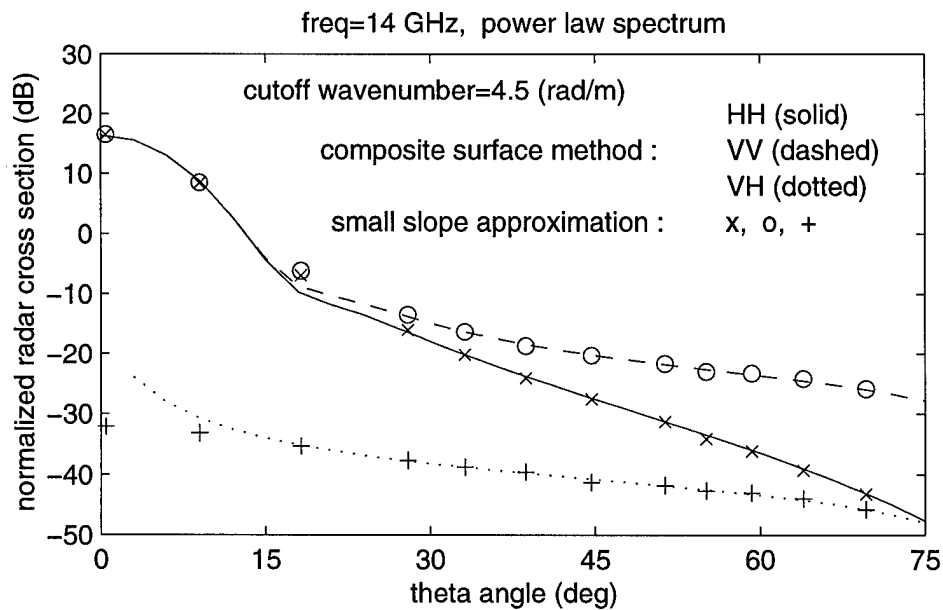Figure 3.1: Comparisons of radar returns for the power law spectrum with low cutoff wavenumber $k/128$.



Figure 3.2: Comparisons of radar returns for the power law spectrum with low cutoff wavenumber $k/64$.

14

# Chapter 4

# Radar Cross Sections for the Durden-Vesecky and Apel Spectra

The Durden-Vesecky and Apel spectral models vary with the wind velocity over the sea surface and thus describe more realistic sea surfaces. To evaluate the effect differing models for the sea surface spectrum can have on sea surface scattering, radar cross sections for the two spectral models are calculated using the composite surface method at five frequencies (1 GHz, 5 GHz, 10 GHz, 14 GHz and 35 GHz) and for three wind speeds ($U_{19.5}$ of 4 m/sec, 12 m/sec and 20 m/sec). Results are illustrated for upwind cross sections and the up-cross wind difference, and also compared with predictions of empirical backscattering models.

## 4.1   Upwind cross sections

Figure 4.1-4.15 compare predictions of backscattering under the composite model for the Durden-Vesecky and Apel spectra versus observation angle. Results at L-band (Figures 4.1-4.3 for wind speeds 4, 12, and 20 m/s, respectively) show significant differences in predictions from the two spectra, with the Apel spectrum generally predicting smaller and larger cross sections for normal and oblique observation, respectively. Larger oblique observation cross sections for the Apel model are consistent with the comparison of Bragg wavenumber amplitudes presented in Chapter 2. Similar results are obtained at C-band (Figures 4.4-4.6), X-band (Figures 4.7-4.9), Ku-band (Figures 4.10-4.12), and Ka band (Figures 4.13-4.15). The two spectra generally are in closest agreement at the lowest wind speed considered, with the exception of L-band, and produce the smallest differences for other wind speeds at C-band. Again,

these results are consistent with the comparison of Bragg wavenumber amplitudes in Chapter 2.

Variations with frequency show somewhat smaller cross sections near normal incidence as frequency increases and somewhat larger cross sections at oblique angles, as should also be expected for surfaces which appear rougher for shorter electromagnetic wavelengths. Cross polarized cross sections are observed to increase significantly with wind speed and slightly with frequency. Note that the cross polarized results should be inaccurate for $\theta_i < 10°$ as discussed in Chapter 3.

### 4.1.1 Normal incidence cross sections

Of some special interest to altimeter applications are radar cross sections at normal incidence. As indicated in equation (2.3), the rms slopes $s_x$ and $s_y$ are important for determining near normal incidence radar returns. Figure 4.16 compares $s_x$ and $\sqrt{s_x s_y}$ associated with the Durden-Vesecky and Apel spectral models for three wind speeds at five frequencies. One can see that $s_x$ and $\sqrt{s_x s_y}$ are always larger for the Apel model than for the Durden-Vesecky model. Thus, from equation (2.3) and Figure 4.16 one can reach the conclusion that near normal incidence, the radar cross section for the Apel model is lower than for the Durden-Vesecky model, and as the incident angle increases away form normal incidence, "tilting" effects will be larger for the Apel model. Normal incidence returns from Figures 4.1 to 4.15 are plotted in Figure 4.17 for both spectral models at the 5 frequencies and 3 wind speeds considered. Radar cross sections at normal incidence are indeed higher for the Durden-Vesecky spectrum than for the Apel spectrum, and results for both spectral models tend to decrease as the wind speed picks up from 4 m/sec and/or the frequency increases from 1 GHz to 35 GHz. Note the frequency dependence for these near specular results is obtained from the choice of $k/2$ as the long wave region cutoff wavenumber, since slope variances are obtained only from the long wave region. Comparisons with empirical altimeter results would be required to assess these predictions in detail.
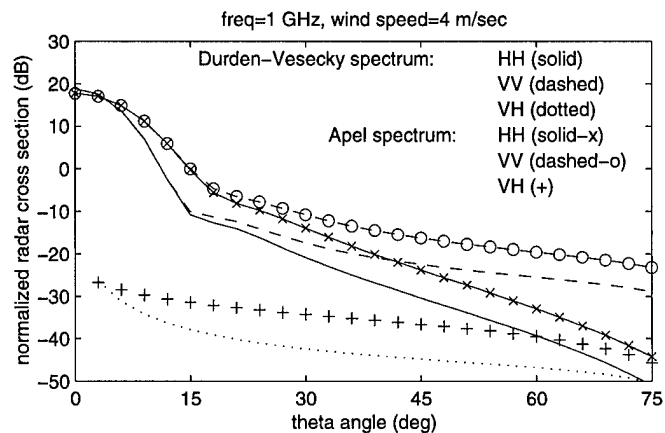
Figure 4.1: Comparisons of radar cross sections in the up-wind direction at 1 GHz with wind speed=4 m/sec.
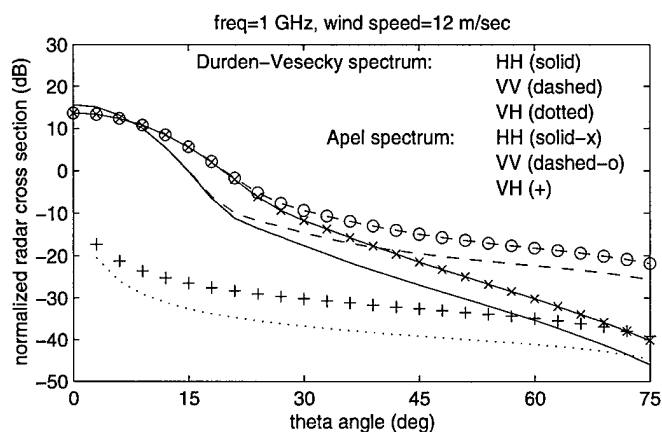


Figure 4.2: Comparisons of radar cross sections in the up-wind direction at 1 GHz with wind speed=12 m/sec.
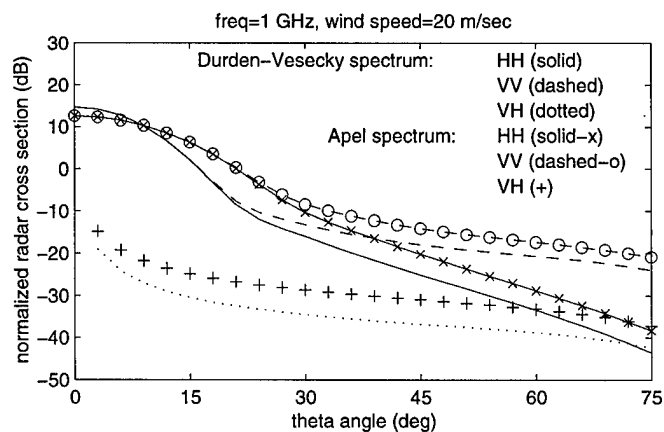


Figure 4.3: Comparisons of radar cross sections in the up-wind direction at 1 GHz with wind speed=20 m/sec.
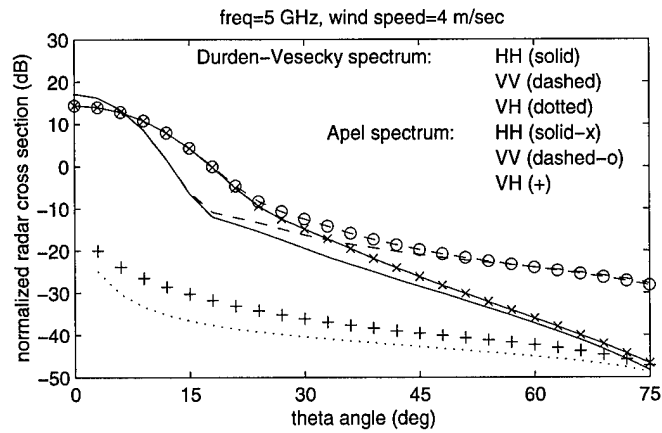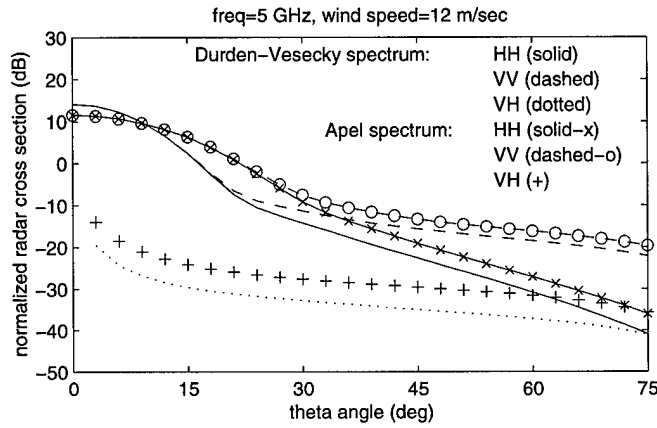
17

Figure 4.4: Comparisons of radar cross sections in the up-wind direction at 5 GHz with wind speed=4 m/sec.



Figure 4.5: Comparisons of radar cross sections in the up-wind direction at 5 GHz with wind speed=12 m/sec.
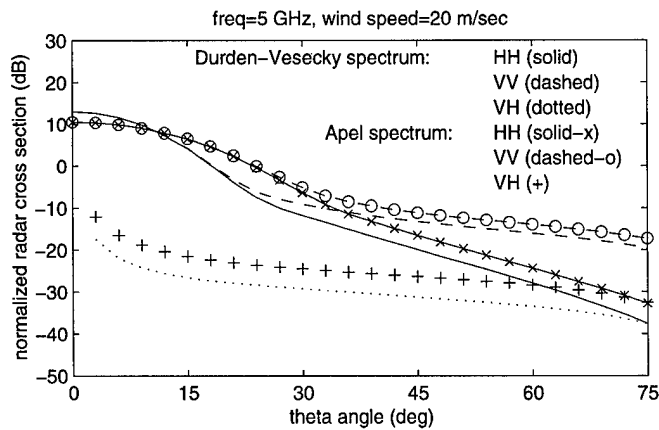


Figure 4.6: Comparisons of radar cross sections in the up-wind direction at 5 GHz with wind speed=20 m/sec.
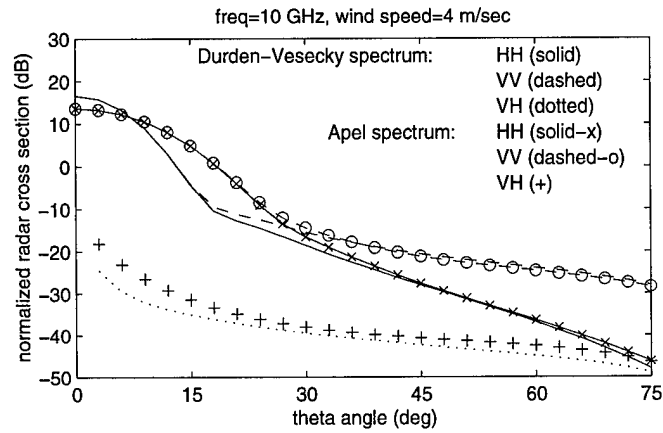
Figure 4.7: Comparisons of radar cross sections in the up-wind direction at 10 GHz with wind speed=4 m/sec.
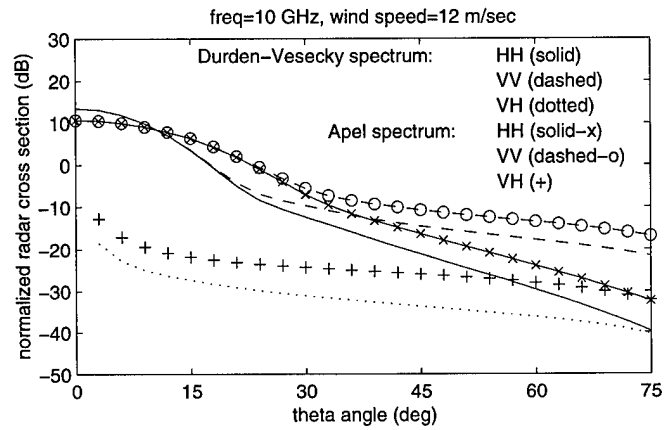


Figure 4.8: Comparisons of radar cross sections in the up-wind direction at 10 GHz with wind speed=12 m/sec.
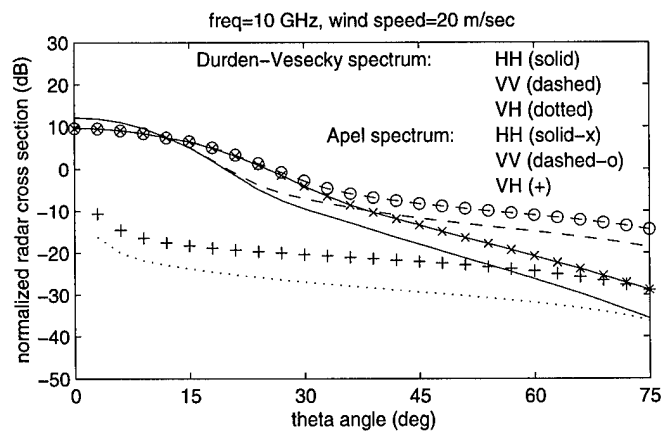


Figure 4.9: Comparisons of radar cross sections in the up-wind direction at 10 GHz with wind speed=20 m/sec.

Figure 4.10: Comparisons of radar cross sections in the up-wind direction at 14 GHz with wind speed=4 m/sec.



Figure 4.11: Comparisons of radar cross sections in the up-wind direction at 14 GHz with wind speed=12 m/sec.
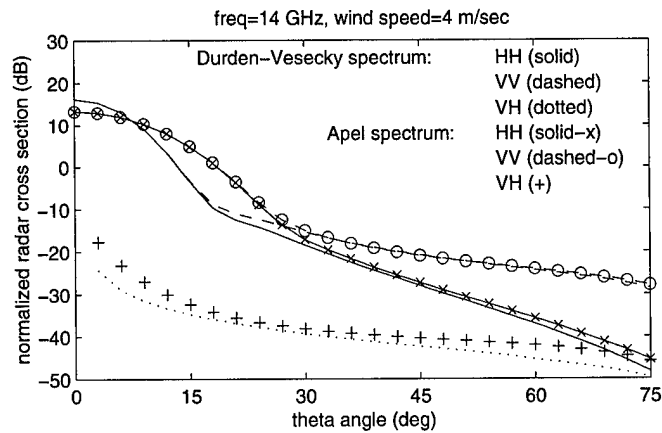


Figure 4.12: Comparisons of radar cross sections in the up-wind direction at 14 GHz with wind speed=20 m/sec.

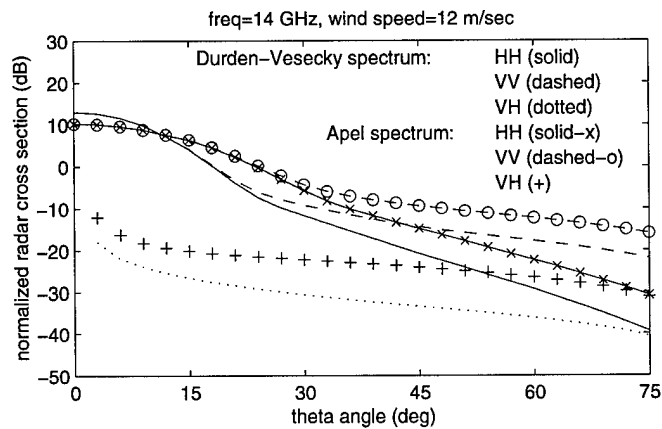Figure 4.13: Comparisons of radar cross sections in the up-wind direction at 35 GHz with wind speed=4 m/sec.



Figure 4.14: Comparisons of radar cross sections in the up-wind direction at 35 GHz with wind speed=12 m/sec.
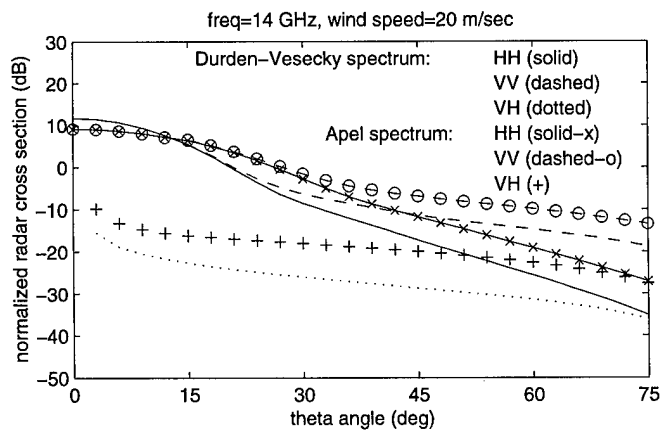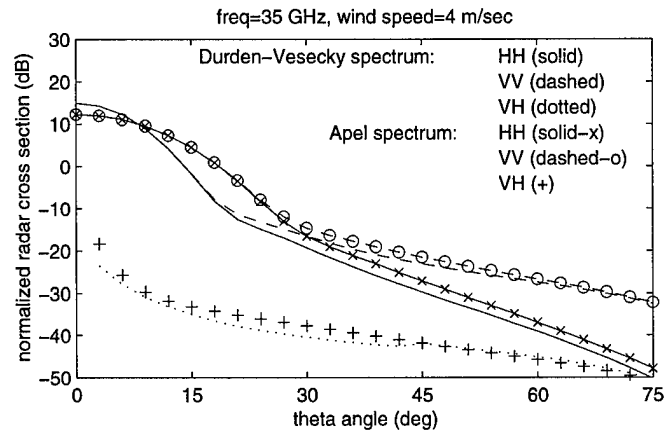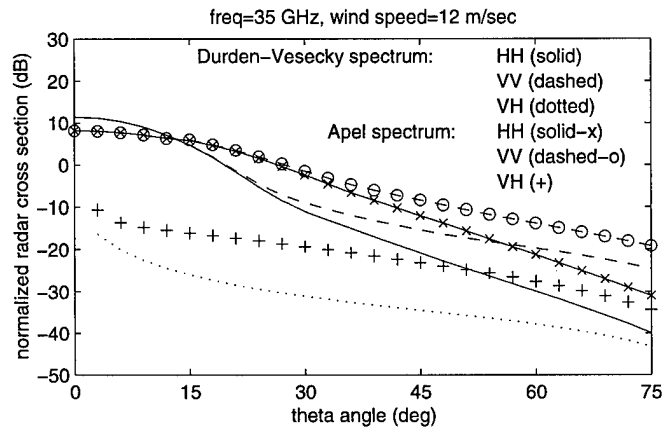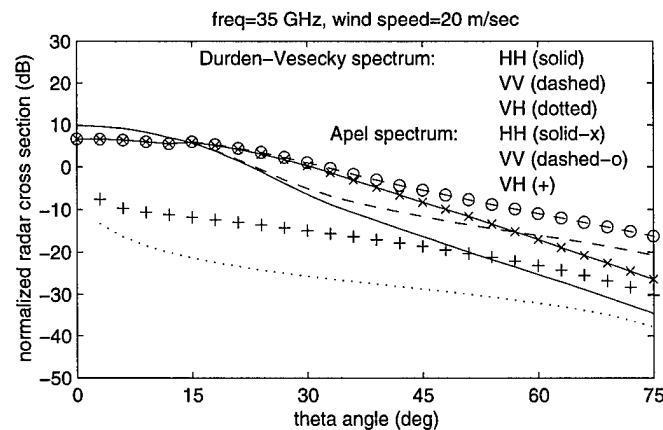


Figure 4.15: Comparisons of radar cross sections in the up-wind direction at 35 GHz with wind speed=20 m/sec.

21
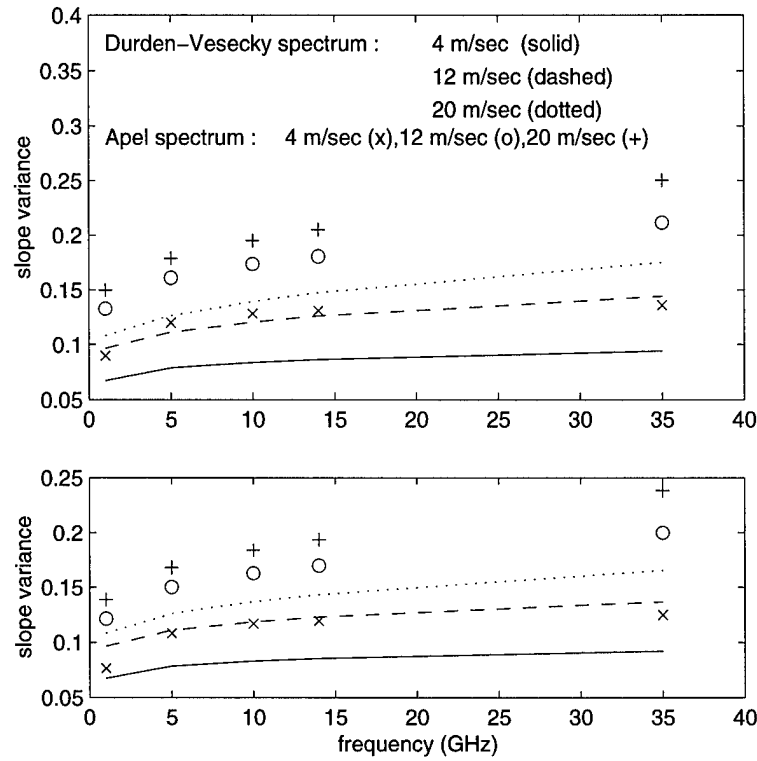
Figure 4.16: Comparisons of rms slopes for the Durden-Vesecky and Apel spectra. The top figure is for $s_x$ and the bottom figure for $\sqrt{s_x s_y}$. (Note that the curves for the Durden-Vesecky spectrum are simply straight line connections of the calculated data points at five frequencies.)



Figure 4.17: Radar cross sections at normal incidence for the Durden-Vesecky and Apel spectra. (Note that the curves for the Durden-Vesecky spectrum are simply straight line connections of the calculated data points at five frequencies.)

Figure 4.18: Wind exponents versus (Bragg) wavenumber obtained directly from spectral models and obtained from Upwind RCS data (a) VV (b) HH

## 4.1.2 Wind speed dependence

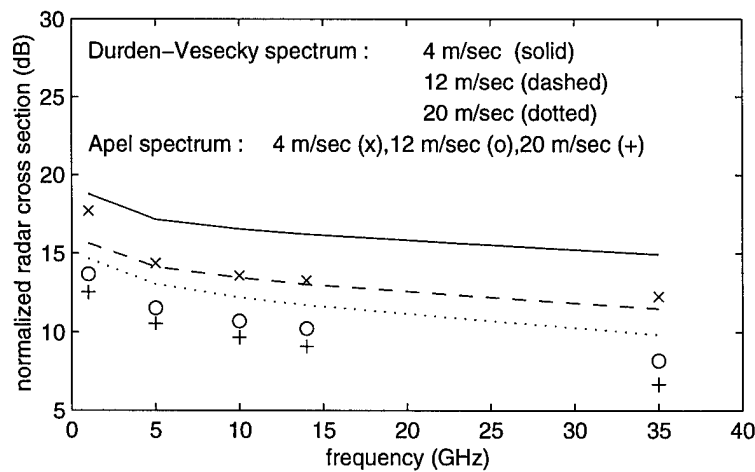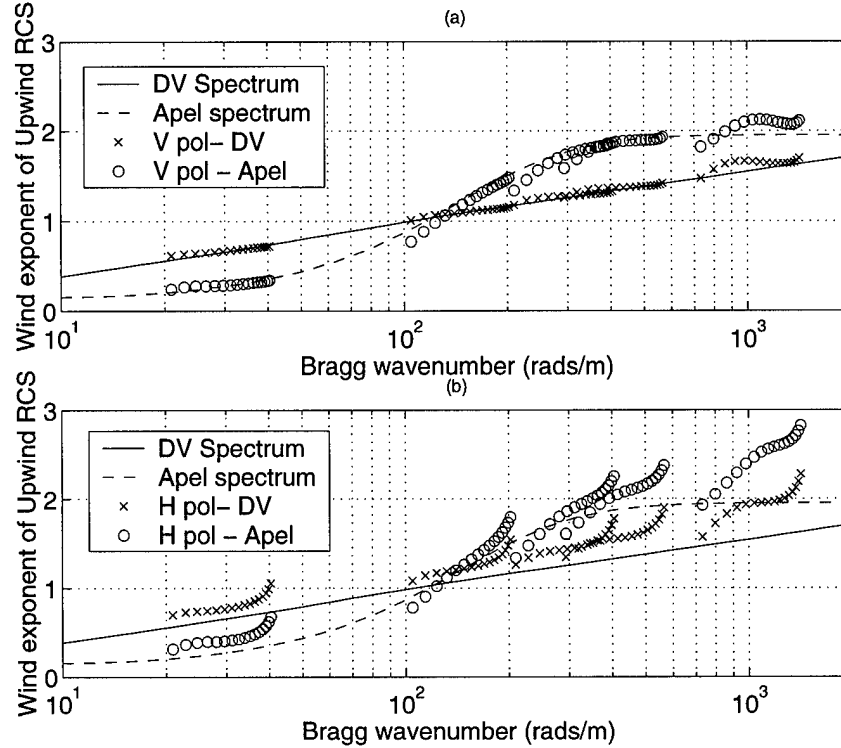The wind dependence of radar cross sections is also of interest, and is typically modeled as $\sigma = aU_{19.5}^b$ ($\sigma$ not in dB) where $a$ and $b$ are constants which vary with frequency and observation angle. Figure 4.18 plots the exponent $b$ versus Bragg wavenumber (a function of frequency and observation angle) derived from fits to upwind RCS data with $30° < \theta_i < 75°$ at wind speeds 4, 8, 12, 16, 20, and 24 m/sec and frequencies 1, 5, 10, 14, and 35 GHz. Results from backscatter data under the two spectral models (symbols) are compared to those obtained directly from the spectra (curves). Exponents derived from $VV$ RCS data are found to be in general agreement with those directly from the spectra, indicating the small influence of tilting effects on $VV$ cross sections. $HH$ results show larger differences since tilting effects are more significant, particularly at the higher frequency end of the Bragg region for a given frequency corresponding to the larger observation angles. The two spectral models predict generally increasing exponents versus wavenumber, although the Durden Vesecky trend is more linear while the Apel model shows a higher order dependency.

## 4.2 Variations with azimuth angle

Figures 4.1 to 4.15 plot radar cross sections when the incident angle $\phi_i$ is in the up wind direction, i.e., $\phi_i = 0$. Usually the difference in the radar cross sections for the cross wind direction ($\phi_i = \pi/2$) and for the up wind direction is small. Thus, instead of showing the radar cross sections for $\phi_i = \pi/2$, which would be very similar to those shown in Figures 4.1 to 4.15, it is more informative to show the difference in the radar cross sections for the two $\phi_i$ angles. To do this, write sea surface radar cross sections (not in decibels) as

$$\sigma = A + B \cos \phi_i + C \cos 2\phi_i, \qquad (4.1)$$

where $A$, $B$ and $C$ are functions of the frequency, wind speed and incident angle $\theta_i$. The first harmonic term $B$ describes an up/down wind asymmetry in radar cross sections, and can be obtained only with a non-Gaussian random process model of the sea surface. For simplicity, first harmonic terms are neglected in this report. The second harmonic term $C$ is responsible for the radar cross section variation in the up wind and cross wind directions. Examples of 2C at 5 GHz and 14 GHz are shown in Figures 4.19 to 4.22. The second harmonic term has larger values for $\theta_i < 30°$ where cross sections in general are larger, and shows variations with polarization similar to those obtained from cross section zeroth azimuthal harmonics $A$. Cross section second harmonics show improved agreement between the two spectral models for oblique observation angles, but near normal incidence results are much larger for the Apel model due to its inclusion of azimuthal variations in the long wave portion of the spectrum.

## 4.3 Comparison with empirical scattering models

It is interesting to see how the radar cross section predictions of the Durden-Vesecky and Apel spectral models compare with some empirical sea surface scattering models. Three representative empirical models in the literature are the CMOD2-I3 [20], SASS-II [21] and NSCAT-I [22] models. The CMOD2-I3 model applies for vertically polarized radar cross sections at 5 GHz; comparisons of upwind cross sections with the composite model are shown in Figures 4.23 to 4.25 for wind speeds 4, 12, and 20 m/sec, respectively. Note the CMOD2-I3 empirical model strictly applies for inci-
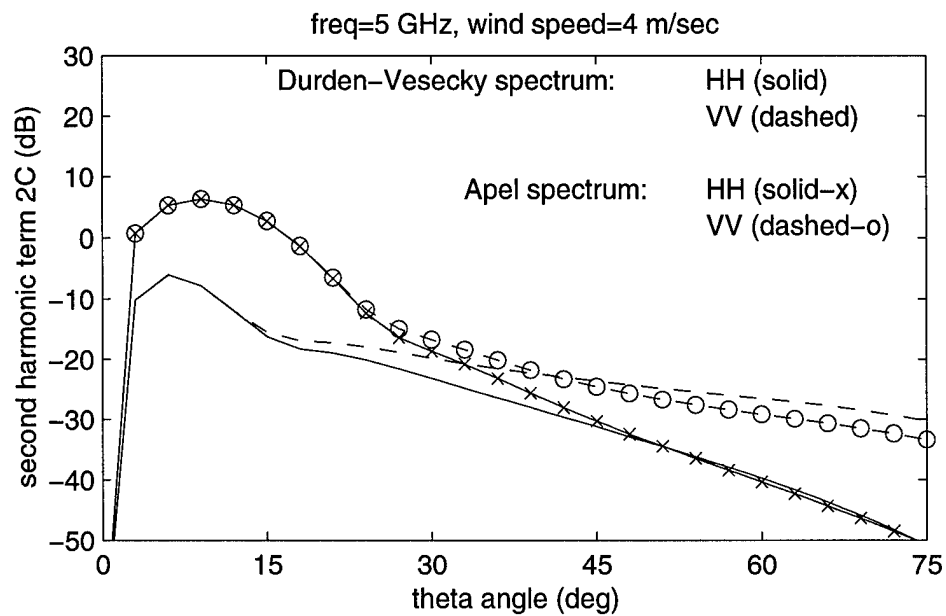
freq=5 GHz, wind speed=4 m/sec

Durden–Vesecky spectrum:     HH (solid)
                             VV (dashed)

Apel spectrum:     HH (solid–x)
                   VV (dashed–o)

Figure 4.19: Differences between the normalized radar cross sections in the upwind and cross wind directions at 5 GHz with wind speed=4 m/sec.



freq=5 GHz, wind speed=12 m/sec

Durden–Vesecky spectrum:     HH (solid)
                             VV (dashed)

Apel spectrum:     HH (solid–x)
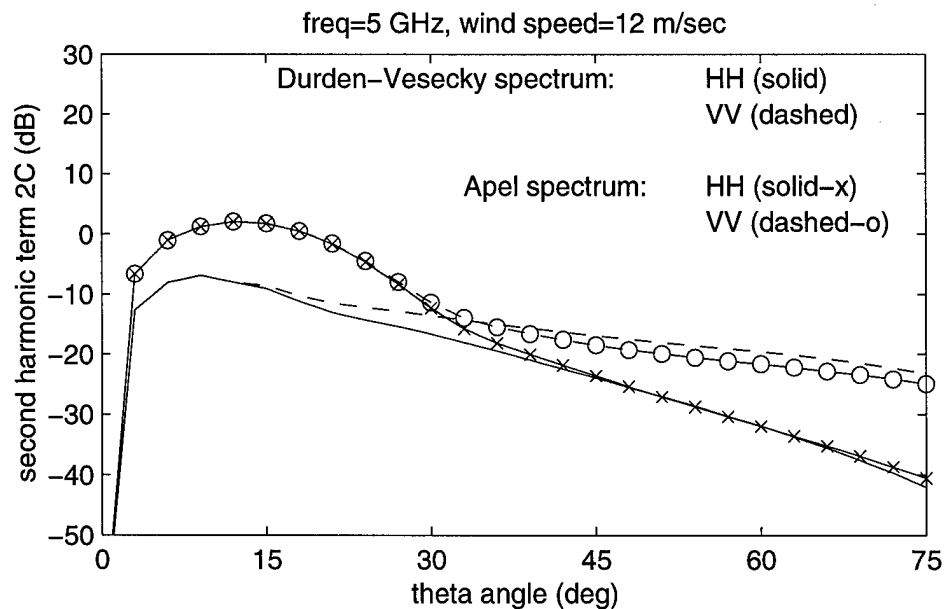                   VV (dashed–o)

Figure 4.20: Differences between the normalized radar cross sections in the upwind and cross wind directions at 5 GHz with wind speed=12 m/sec.
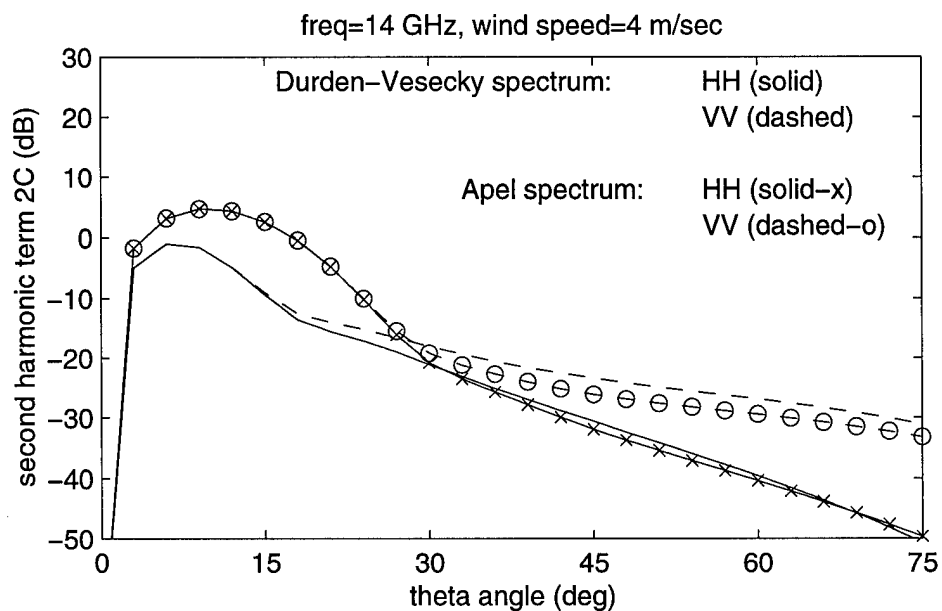
Figure 4.21: Differences between the normalized radar cross sections in the upwind and cross wind directions at 14 GHz with wind speed=4 m/sec.
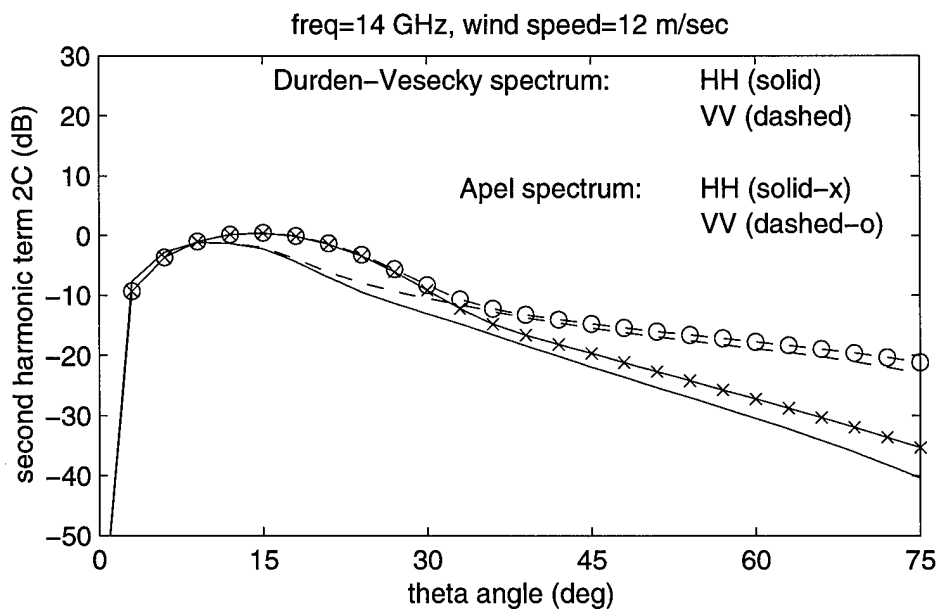


Figure 4.22: Differences between the normalized radar cross sections in the upwind and cross wind directions at 14 GHz with wind speed=12 m/sec.

26

dence angles $\theta_i$ in the range $18° < \theta_i < 58°$ only even though the empirical curves are plotted outside this range. Results show excellent agreement between the empirical model and cross sections from the Apel spectrum, while Durden-Vesecky spectrum results underpredict the CMOD2-I3 model. Second azimuthal harmonic results are compared in Figures 4.26 to 4.27 for wind speeds 4 and 12 m/sec, respectively, and produce similar conclusions. The success of the Apel spectrum in matching CMOD2-I3 results suggests that the C-band Bragg portion of the spectrum is being modeled reasonably well by the Apel spectrum, although complete conclusions in this regard are difficult to obtain due to the interplay of Bragg scatter and "tilting" effects.

The SASS-II and NSCAT-I empirical models provide predictions of both horizontal and vertical co-pol cross sections at 14 GHz for observation angles $0 < \theta_i < 60°$ and $15° < \theta_i < 65°$, respectively. These models provide similar but slightly differing predictions since they were derived from observations with different sensors. Comparisons with the SASS-II model for up-wind cross sections at 4 and 12 m/s are provided in Figures 4.28 to 4.29 and for up/cross wind differences in Figures 4.30 to 4.31. The comparison shows empirical predictions generally to fall between those from the Durden Vesecky and Apel spectral models, although vertically polarized cross sections are somewhat closer to those from the Durden Vesecky spectrum. The large up/cross wind differences obtained from the Apel spectrum for small incidence angles are not predicted by the SASS-II model, suggesting that some of the Apel spectrum azimuthal description in the long wave region may be inaccurate. Comparisons with the NSCAT-1 model in Figures 4.32 to 4.35 yield similar results.
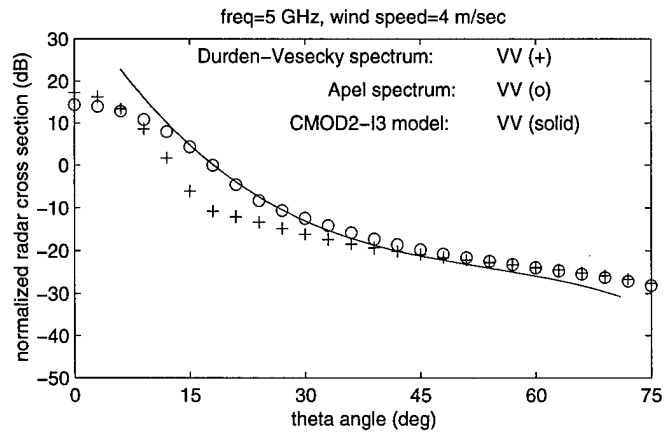
Figure 4.23: Vertical polarization radar cross sections in the up wind direction at 5 GHz with wind speed=4 m/sec.
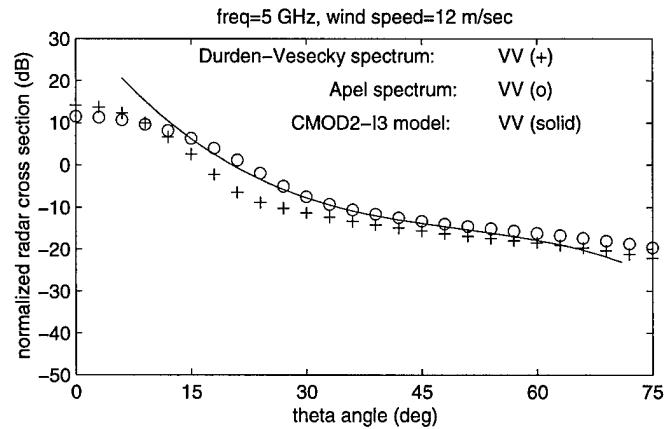


Figure 4.24: Vertical polarization radar cross sections in the up wind direction at 5 GHz with wind speed=12 m/sec.
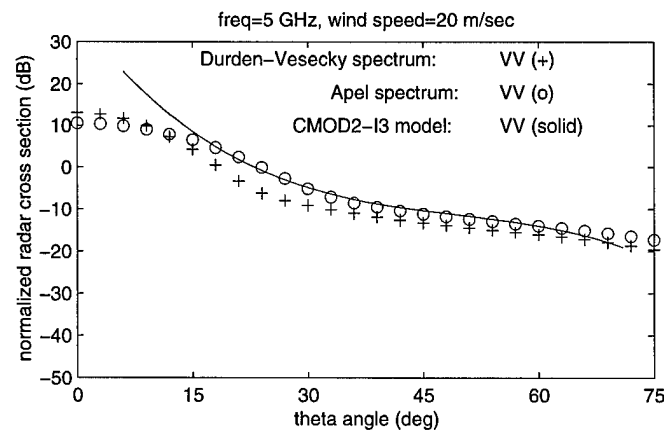


Figure 4.25: Vertical polarization radar cross sections in the up wind direction at 5 GHz with wind speed=20 m/sec.
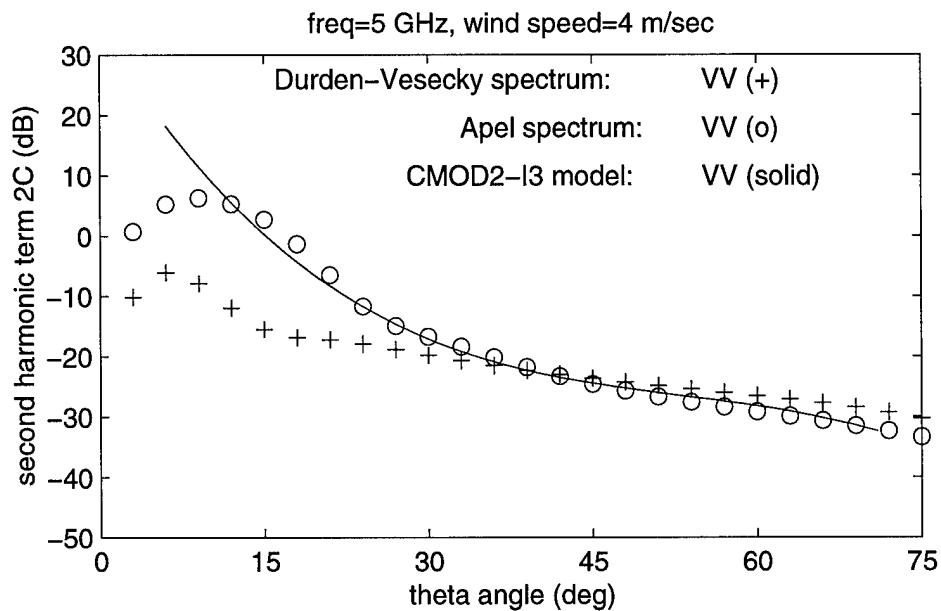
Figure 4.26: Differences between the vertical polarization radar cross sections in the up-wind and cross-wind directions at 5 GHz with wind speed=4 m/sec.
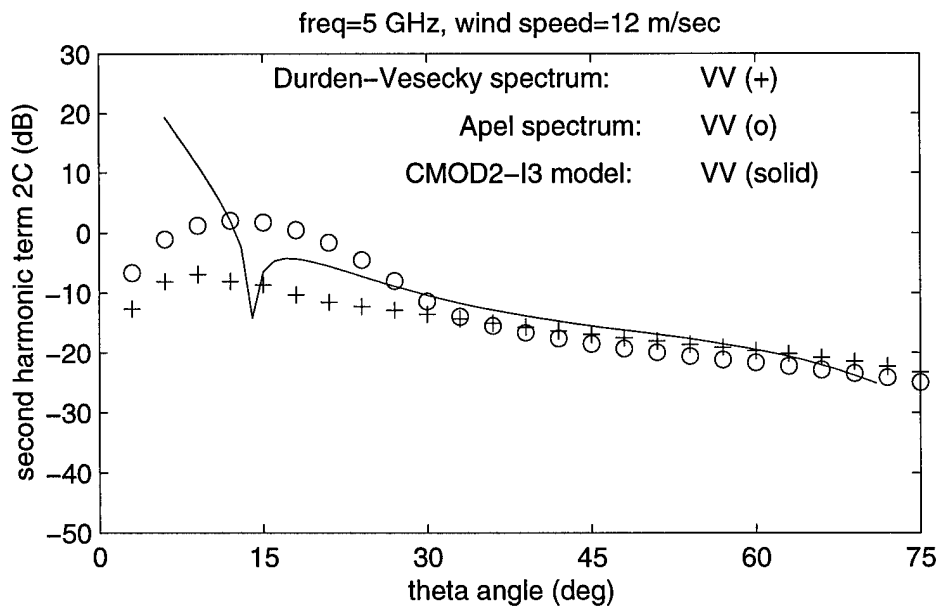


Figure 4.27: Differences between the vertical polarization radar cross sections in the up-wind and cross-wind directions at 5 GHz with wind speed=12 m/sec.

Figure 4.28: Radar cross sections in the up-wind direction at 14 GHz with wind speed=4 m/sec.

Figure 4.29: Radar cross sections in the up-wind direction at 14 GHz with wind speed=12 m/sec.

Figure 4.30: Differences between the radar cross sections in the up-wind and cross-wind directions at 14 GHz with wind speed=4 m/sec.

Figure 4.31: Differences between the radar cross sections in the up-wind and cross-wind directions at 14 GHz with wind speed=12 m/sec.
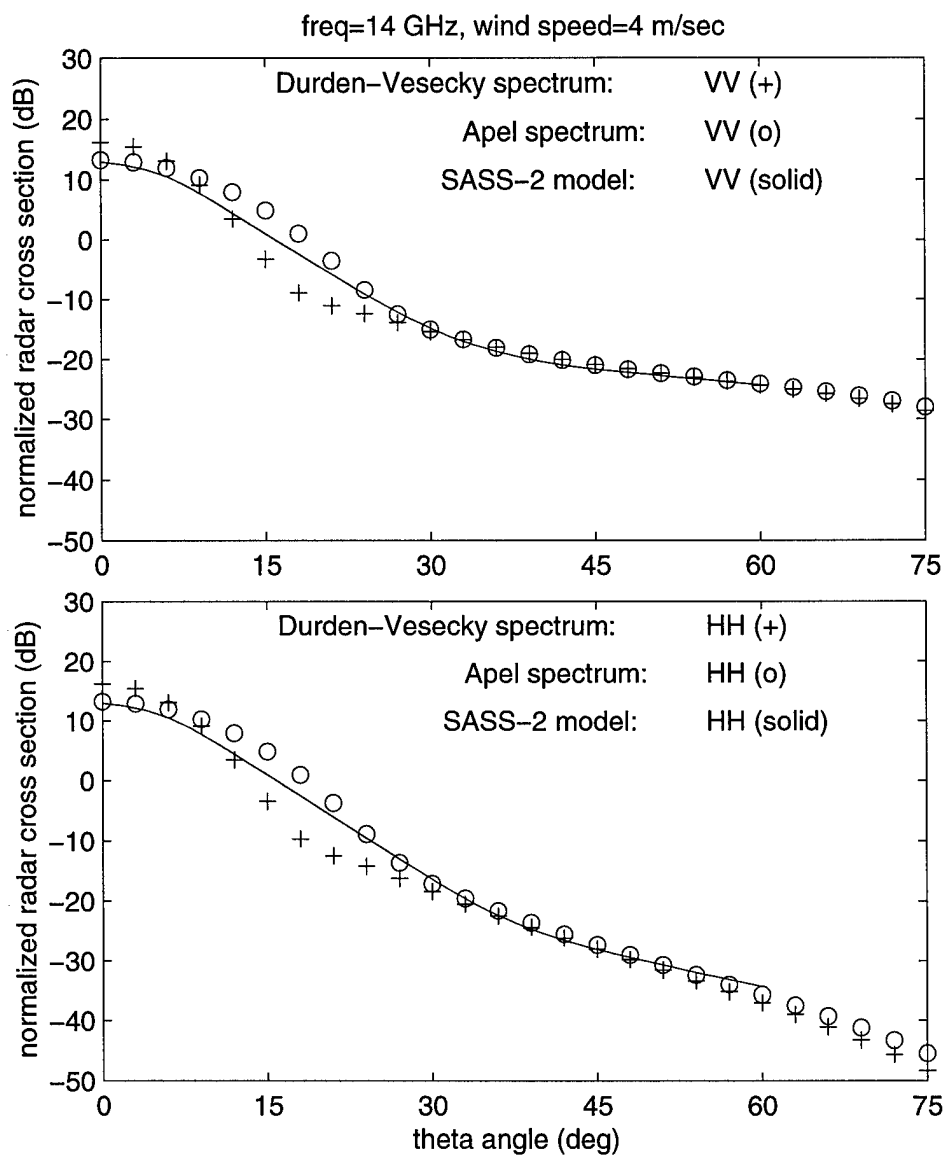
Figure 4.32: Radar cross sections in the up-wind direction at 14 GHz with wind speed=4 m/sec.
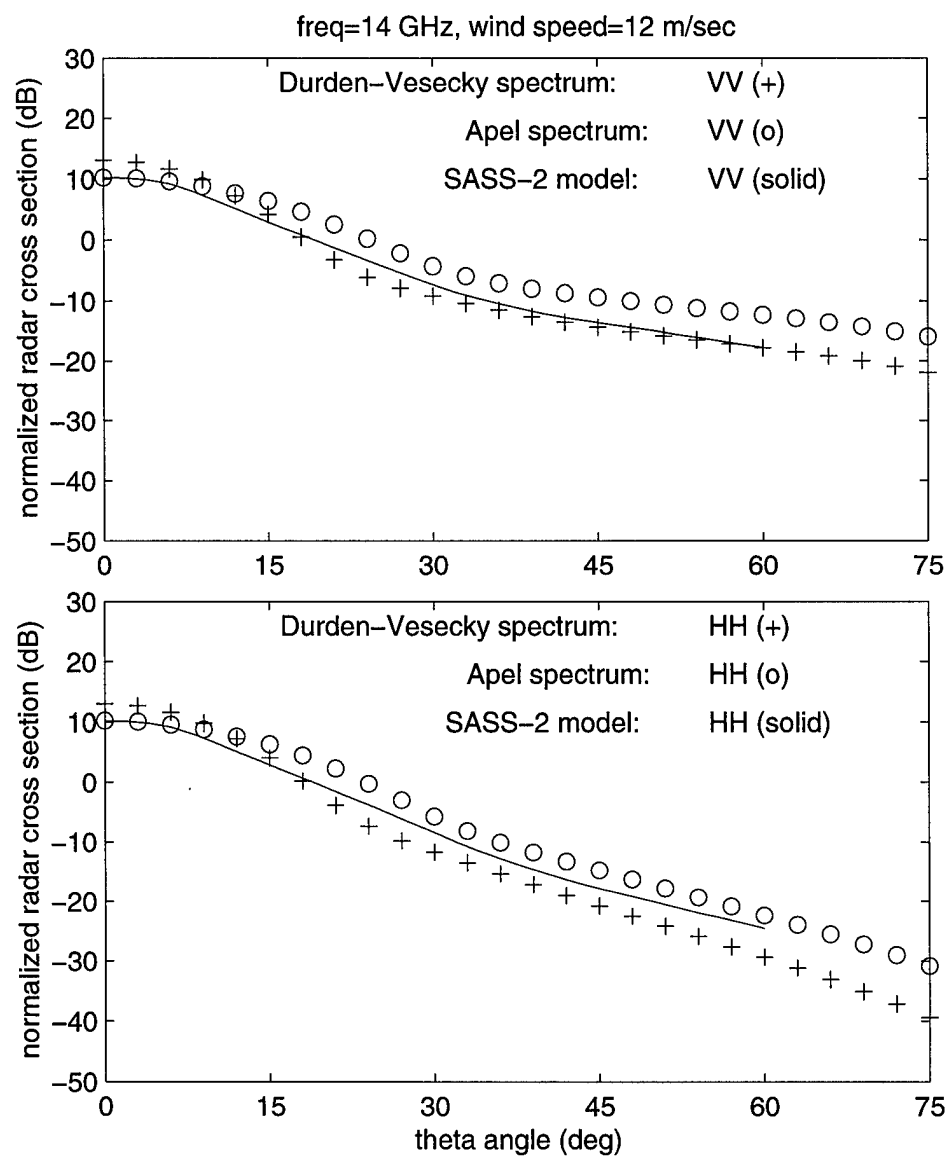
Figure 4.33: Radar cross sections in the up-wind direction at 14 GHz with wind speed=12 m/sec.
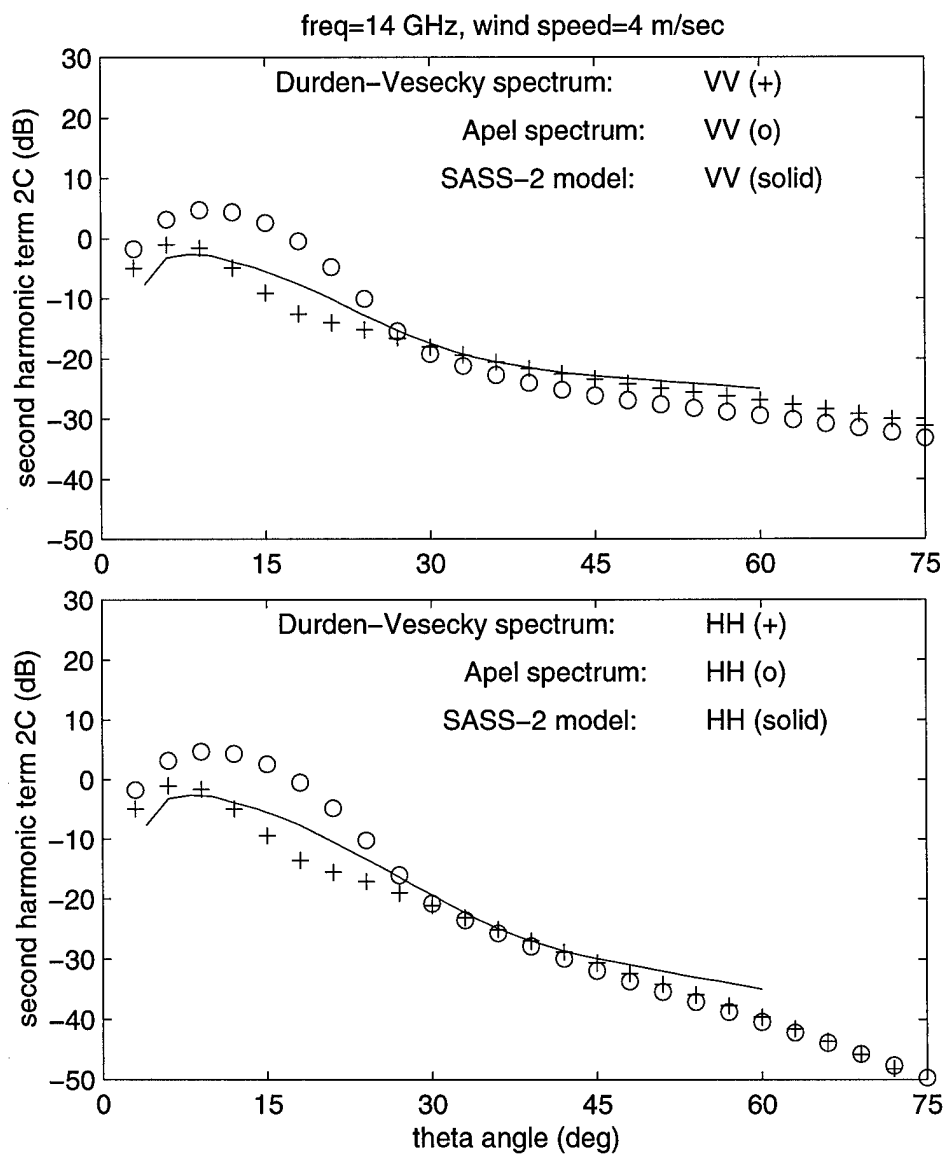
Figure 4.34: Difference between the radar cross sections in the up-wind and cross-wind directions at 14 GHz with wind speed=4 m/sec.
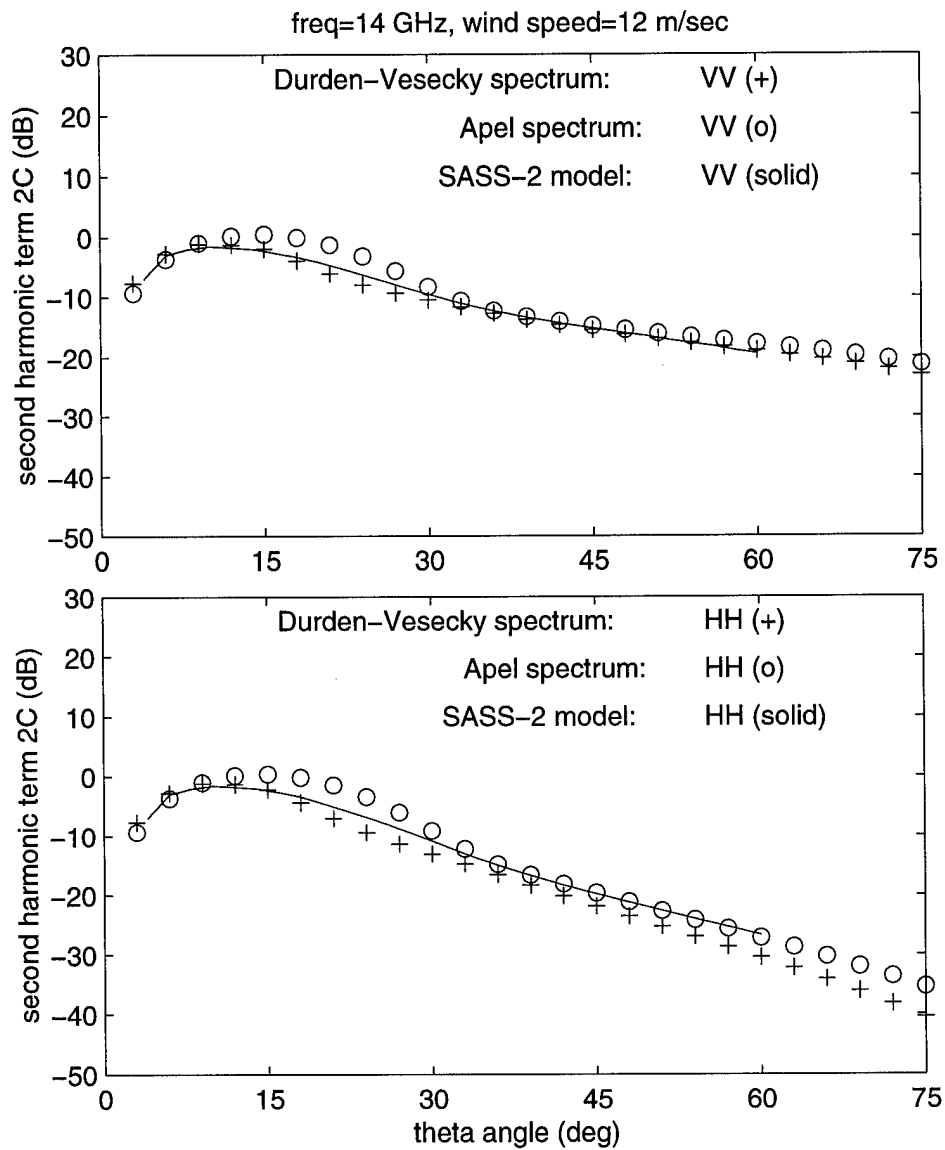
Figure 4.35: Differences between the radar cross sections in the up-wind and cross-wind directions at 14 GHz with wind speed=12 m/sec.
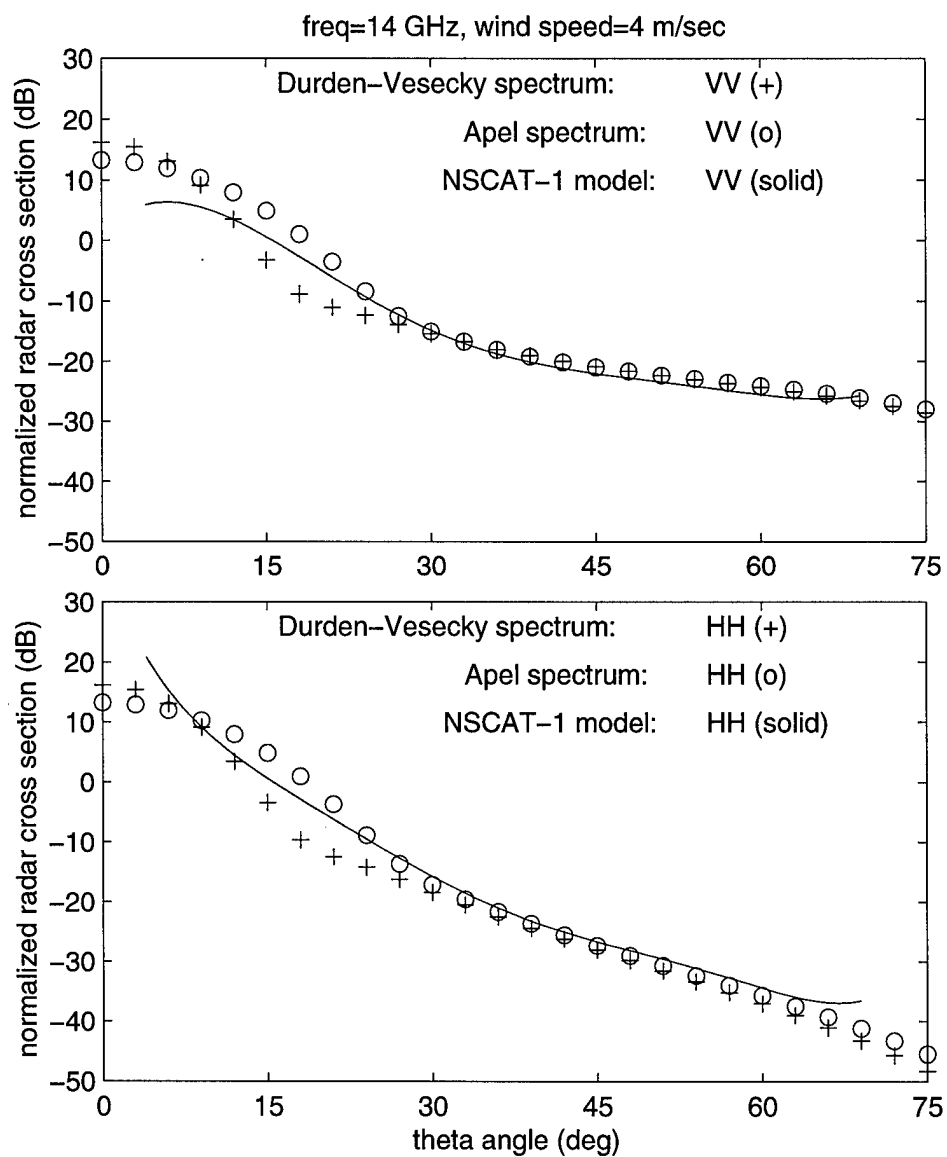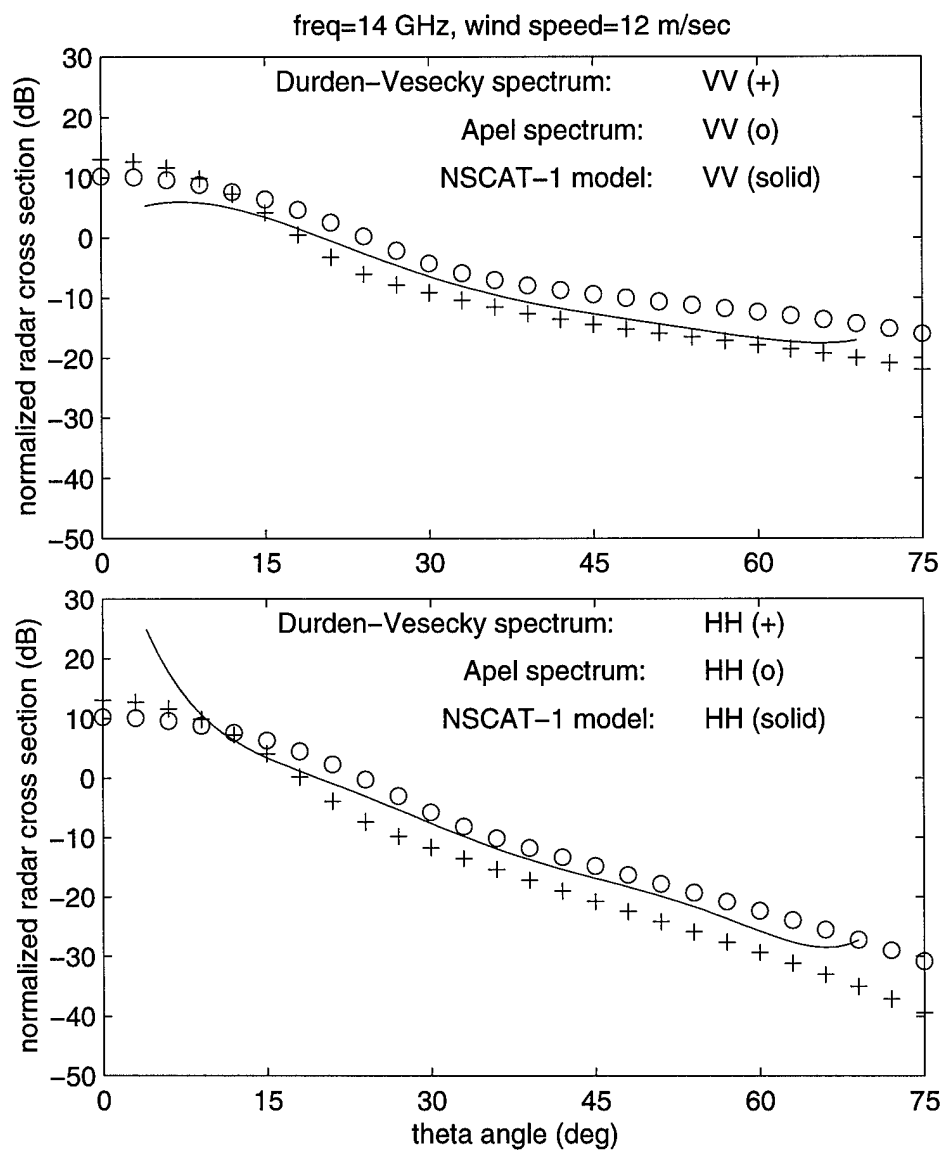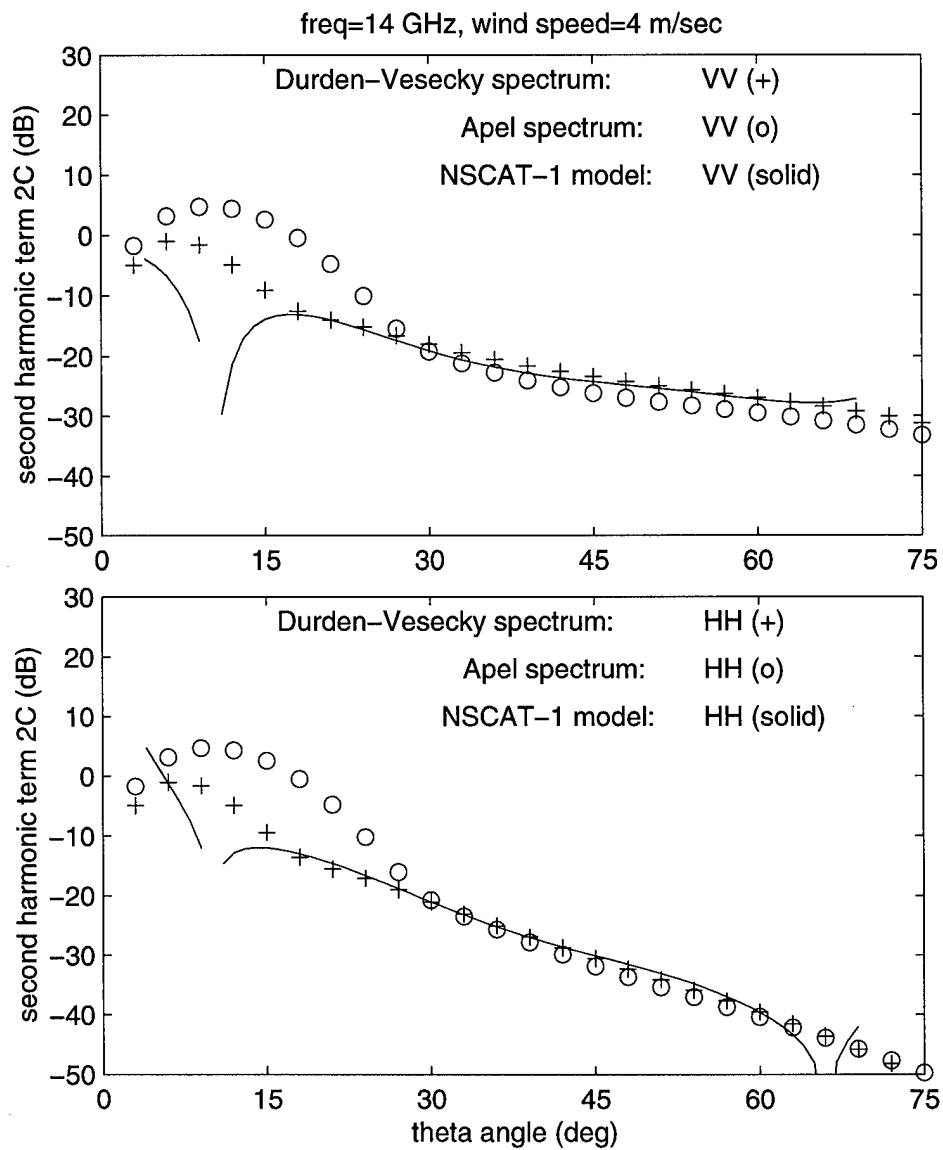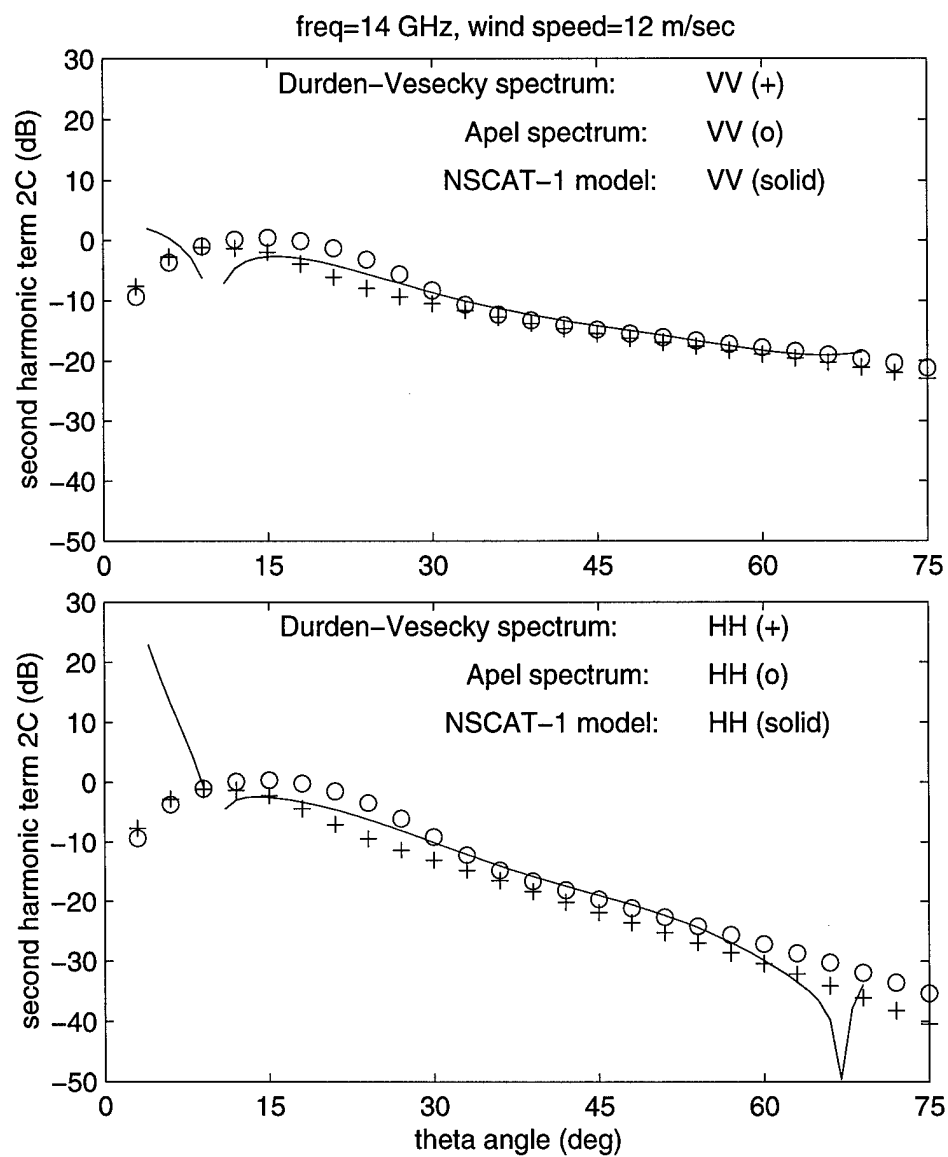
# Chapter 5

# Conclusions

The composite surface method has been employed to evaluate sea surface backscattering of three ocean surface spectral models. Radar cross sections for the power law spectrum were found to agree well with those calculated by the small slope approximation, validating the composite surface model for prediction of scattering from ocean-like surfaces. The Durden-Vesecky and Apel spectral models were then applied to describe more realistic sea surfaces which vary in azimuth and with wind speed. These two models were found however to differ in their description of the short gravity-capillary portion of the spectrum and in surface azimuthal dependency. Radar cross sections calculated from the two models generally showed large differences, indicating the importance of the surface spectral model used for sea surface scattering predictions. Comparisons with empirical scattering models showed the Apel model to provide better agreement for C-band results, while empirical predictions generally were between those from the two spectral models at Ku band. Further comparisons with a larger set of empirical results can help to clarify the successes and failures of these spectral models, and will be considered in future efforts. Future studies will also include additional directional spectrum models to evaluate their performance, and will investigate sea surface thermal emission effects as well.

# Bibliography

[1] M.I. Skolnik, *Introduction to Radar Systems*, Second edition, McGraw-Hill, New York, 1980.

[2] L.B. Wetzel, "Sea Clutter," chapter 13 of *Radar Handbook*, second edition, M. Skolnik, ed., McGraw-Hill, New York, 1990.

[3] J.W. Wright, "A new model for sea clutter," *IEEE Trans. Antennas Propagat.*, vol. AP-16, pp. 217-223, 1968.

[4] D. Barrick and W. Peake, "A review of scattering from surfaces with different roughness scales," *Radio Sci.*, vol. 3, pp. 865-868, 1968.

[5] G.R. Valenzuela, "Theories for the interaction of electromagnetic and oceanic waves: a review," *Bound. Layer Meteorology*, vol. 13, pp. 61-85, 1978.

[6] J.T. Johnson, "A numerical study of low grazing angle backscatter from ocean-like impedance surfaces with the canonical grid method," *IEEE Trans. Antennas Propagat.*, vol. 46, no. 1, Jan. 1998.

[7] S.L. Durden and J.F. Vesecky, "A physical radar cross-section model for a wind driven sea with swell," *IEEE J. Oceanic Eng.*, vol. OE-10, pp. 445-451, 1985.

[8] J.R. Apel, "An improved model of the ocean surface wave vector spectrum and its effects on radar backscatter," *J. Geophys. Res.*, vol. 99, pp. 16269-16291, 1994.

[9] A.G. Voronovich, *Wave Scattering from Rough Surfaces*, Berlin: Springer-Verlag, 1994.

[10] Hwang, P. A., "A study of the wavenumber spectra of short water waves in the ocean. Part 2: Spectral model and mean square slope," *J. Atmos. and Oceanic Tech.*, vol. 14, pp. 1174-1186, 1997.

[11] Hwang, P.A., S. Atakturk, M. A. Sletten, and D. B. Trizna, "A study of the wavenumber spectra of short water waves in the ocean," *J. Phys. Oceanogr.*, vol. 26, pp. 1266-1285, 1996.

[12] J.T. Johnson, R.T. Shin, J.A. Kong, L. Tsang and K. Pak, "A numerical study of the composite surface model for ocean scattering," *IEEE Trans. Geosc. Remote Sens.*, vol. 36, pp. 72-83, 1998.

[13] G.R. Valenzuela, "Scattering of electromagnetic waves from a tilted slightly rough surface," *Radio Sci.*, vol. 3, pp. 1057-1066, 1968.

[14] G.R. Valenzuela, "Depolarization of EM waves by slightly rough surfaces," *IEEE Trans. Ant. Prop.*, vol. 15, pp. 552-557, 1967.

[15] Elfouhaily, T., B. Chapron, K. Katsaros, and D. Vandemark, "A unified directional spectrum for long and short wind-driven waves," *J. Geophys. Res.*, vol. 102, pp. 15780–15796, 1997.

[16] Hwang, P. A., D. W. Wang, E. J. Walsh, W. B. Krabill, and R. N. Swift, "Airborne measurements of the wavenumber spectra of ocean surface waves. Part 1. Spectral slope and nondimensional spectral coefficient," To appear, *J. Phys. Oceanogr.*, 1999.

[17] Hwang, P. A., D. W. Wang, E. J. Walsh, W. B. Krabill, and R. N. Swift, "Airborne measurements of the wavenumber spectra of ocean surface waves. Part 2. Directional distribution," To appear, *J. Phys. Oceanogr.*, 1999.

[18] Voronovich, A. G., "A two scale model from the point of view of the small slope approximation," *Waves in Random Media,* vol. 6, pp. 73–83, 1996.

[19] McDaniel, S. T., "Acoustic and radar scattering from directional seas," *Waves in Random Media,* vol. 9, no. 4, pp. 537–549, 1999.

[20] A. Bentamy, P. Queffeulou, Y. Quilfen and K. Katsaros, "Ocean surface wind fields estimated from satellite active and passive microwave instruments," *IEEE Trans. Geosci. Remote Sens.*, vol. 37, pp. 2469-2486, 1999.

[21] F.J. Wentz, S. Peteherych, and L.A. Thomas, "A model function for ocean radar cross sections at 14.6 GHz," *J. of Geophys. Research,* vol. 89, pp. 3689-3704, 1984.

[22] F.J. Wentz and D.K. Smith, "A model function for the ocean-normalized radar cross-section at 14 GHz derived from NSCAT observations," *J. of Geophys. Research,* vol. 104, pp. 11499-11514, 1999.